Received: 16 June 2023 | Revised: 15 December 2023 | Accepted: 18 December 2023

DOI: 10.1111/jmg.12759

ORIGINAL ARTICLE

Journal of METAMORPHIC GEOLOGY WILEY

Paleoarchean metamorphism in the Acasta Gneiss Complex: Constraints from phase equilibrium modelling and in situ garnet Lu–Hf geochronology

Jonas Kaempf[1] | **Tim E. Johnson**[1] | **Chris Clark**[1] | **Julian Alfing**[1] | **Michael Brown**[2] | **Pierre Lanari**[3] | **Kai Rankenburg**[4]

[1]School of Earth and Planetary Sciences, Curtin University, Perth, WA, Australia

[2]Laboratory for Crustal Petrology, Department of Geology, University of Maryland, Maryland, USA

[3]Institute of Geological Sciences, University of Bern, Bern, Switzerland

[4]John de Laeter Centre, Curtin University, Perth, WA, Australia

Correspondence

Jonas Kaempf, School of Earth and Planetary Sciences, Curtin University, Perth, WA 6845, Australia.

Email: jonas.kampf@postgrad.curtin.edu.au

Funding information

Australian Research Council, Grant/Award Number: DP200101104; Curtin University

Handling Editor: Prof. Johann Diener

Abstract

The oldest known evolved (felsic) rocks on Earth (*c.* 4.03 Ga) are found in the Acasta Gneiss Complex (AGC) in north-western Canada and represent a fundamental keystone in unravelling the geological processes governing crustal growth and differentiation during the Hadean and early Archean. Although the timing of multiple episodes of magmatism, metamorphism and deformation in these tonalitic gneisses has been investigated extensively, the metamorphic pressure–temperature (*P*–*T*) conditions recorded by the rocks are poorly constrained. Here, we use phase equilibrium modelling coupled with in situ garnet Lu–Hf geochronology and trace element analysis for two garnet-bearing tonalitic gneisses to decipher the metamorphic history of the AGC. The observed mineral assemblages are consistent with peak metamorphic conditions of $T = 725$–780°C and $P = 4.5$–6.2 kbar and the generation of a small amount of melt (<7 vol.%). Garnet geochronology constrains the age of metamorphism to 3.3–3.2 Ga, consistent with previous evidence for a late Paleoarchean tectono-metamorphic event in the AGC. Subsequent isotopic disturbance of garnet at *c.* 1.9 Ga is interpreted to correspond to a modification of the primary Lu–Hf systematics in response to garnet resorption/recrystallization during the Paleoproterozoic Wopmay orogeny, resulting in significant scatter between these two age components. Our study adds to the small number of published *P*–*T* data for metamorphic rocks older than 2.8 Ga and shows that tonalitic gneisses in the AGC record a high apparent thermal gradient of ~140°C/kbar in the late Paleoarchean. This thermal gradient is the highest among the limited dataset, but is broadly similar to data from other Paleoarchean-Mesoarchean crustal rocks in recording high *T*/*P* ratios (>77.5°C/kbar).

KEYWORDS

Acasta Gneiss Complex, Archean metamorphism, Lu–Hf garnet geochronology, phase equilibrium modelling, *P*–*T* conditions

This is an open access article under the terms of the Creative Commons Attribution-NonCommercial License, which permits use, distribution and reproduction in any medium, provided the original work is properly cited and is not used for commercial purposes.

© 2024 The Authors. *Journal of Metamorphic Geology* published by John Wiley & Sons Ltd.

1 | INTRODUCTION

Deciphering the mechanisms of formation of ancient continental crust and its evolution to form stable cratons are keys to understanding geodynamic processes operating in the late Hadean and Archean (e.g., Bédard, 2018; Brown et al., 2020; Hastie et al., 2016; Johnson et al., 2014, 2017; Korenaga, 2021; Miocevich et al., 2022; Moyen, 2011; Palin, White, Green, Diener, et al., 2016). However, direct constraints on Earth's earliest history are sparse and commonly derived from rocks that have undergone multistage reworking and recrystallization during subsequent tectono-thermal events (Moyen & Martin, 2012; Wiemer et al., 2018). Constraining the timing (*t*) and pressure–temperature (*P*–*T*) conditions of metamorphism in such polymetamorphic terranes is challenging and requires careful evaluation of microstructural, geochemical and isotopic data in an effort to unravel their early history.

Recent compilations of published *P*–*T* data utilizing the thermobaric ratio (*T*/*P*) of metamorphic rocks through time to investigate secular changes in crustal metamorphism have been used to argue that a change from unimodal to bimodal metamorphism since the Archean relates to a change in fundamental geodynamic processes on Earth (Brown & Johnson, 2018, 2019; Holder et al., 2019). Although *P*–*T*–*t* data from metamorphic rocks of Phanerozoic, Proterozoic and late Archean age are abundant, there are few data from rocks metamorphosed prior to 2.8 Ga. This scarcity of *P*–*T* information for Mesoarchean and older metamorphic rocks limits interpretation of early Earth geodynamics and highlights the necessity for further investigations of such ancient terranes to determine the thermal conditions in the early Archean crust.

The Acasta Gneiss Complex (AGC) in north-western Canada is known to have been affected by multiple tectono-metamorphic events during the Archean, some of which reached *P*–*T* conditions sufficiently high to cause anatexis in the felsic gneisses (Iizuka et al., 2007; Moorbath et al., 1997; Stern & Bleeker, 1998). However, despite the importance of the AGC to understanding the early Earth, studies specifically targeting the metamorphic evolution of these gneisses are scarce (e.g., Fisher et al., 2020) and quantitative *P*–*T* constraints are absent. Previous studies in the AGC have been directed towards addressing the petrogenesis and evolution of the oldest crustal component, the Idiwhaa tonalitic gneiss (Reimink et al., 2014), primarily through investigations of the isotopic systematics recorded in zircon (Kirkland et al., in review; Aarons et al., 2020; Bauer et al., 2017, 2020; Bowring & Housh, 1995; Iizuka et al., 2009; Rayner et al., 2005; Reimink et al., 2014; Reimink, Chacko, et al., 2016; Reimink, Davies, et al., 2016). These studies show that AGC zircons typically preserve a complex evolution involving multiple episodes of magmatism, metamorphism and recrystallization. Deciphering the complex internal zircon textures is further impeded by extensive radiation damage (metamictization) and episodes of lead loss, making interpretations of the timing of distinct tectono-metamorphic events ambiguous (Kirkland et al., 2020). Furthermore, zircon geochronology only allows for limited correlation between age data and *P*–*T* estimates, demonstrating the need for additional geochronometers to constrain the timing of metamorphism.

A characteristic feature of the Idiwhaa tonalitic gneiss is the presence of metamorphic garnet, a mineral that is rarely found in other lithologies of the AGC (e.g., Guitreau et al., 2014; Iizuka et al., 2007). Recent developments in reaction cell and laser-ablation inductively coupled plasma mass spectrometry (LA–ICP–MS/MS) permit in situ Lu–Hf isotopic analysis of garnet (Simpson et al., 2021), providing the means to directly link the metamorphic age to a mineral assemblage and the *P*–*T* conditions at which garnet formed. Here, we present quantitative constraints for two garnet-bearing tonalitic gneisses, with a focus on linking metamorphic *P*–*T* conditions to garnet ages to identify distinct tectono-metamorphic events affecting the AGC. We use petrographic observations and mineral chemistry coupled with phase equilibrium modelling and in situ garnet Lu–Hf geochronology to show that these rocks preserve evidence for a late Paleoarchean high-grade metamorphic event that induced limited partial melting and potential resetting of bulk-rock isotopic compositions in the AGC. Lastly, we discuss our results in the context of the limited *P*–*T*–*t* data from localities with metamorphic rocks formed before 2.8 Ga.

2 | GEOLOGICAL BACKGROUND

The Acasta Gneiss Complex, located at the western margin of the Slave Province in north-western Canada (Figure 1a), comprises several suites of igneous rocks that were extensively deformed and metamorphosed during the early and middle Archean, forming a complex assembly of foliated tonalitic and granitic gneisses with subordinate mafic and ultramafic rocks (Bowring & Housh, 1995). Included in the AGC are the oldest known felsic rocks on Earth, the Idiwhaa tonalitic gneisses, which have yielded igneous crystallization ages dating back to the late Hadean (Bowring, King, et al., 1989; Bowring & Williams, 1999; Bowring, Williams, & Compston, 1989; Stern & Bleeker, 1998). Following their discovery during preliminary mapping of the region by the Geological Survey of Canada (Bowring, King,

15251314, 2024, 3, Downloaded from https://onlinelibrary.wiley.com/doi/10.1111/jmg.12759 by Universitat Bern, Wiley Online Library on [13/03/2024]. See the Terms and Conditions (https://onlinelibrary.wiley.com/terms-and-conditions) on Wiley Online Library for rules of use; OA articles are governed by the applicable Creative Commons License

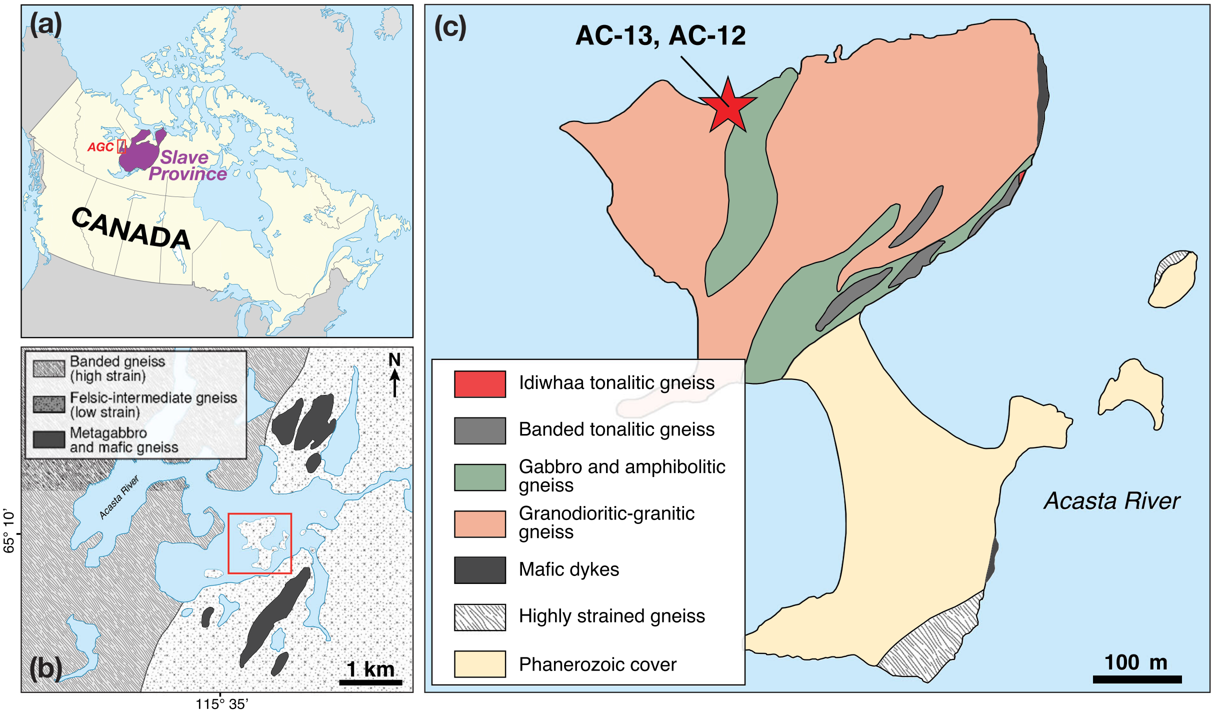

FIGURE 1 (a) Map of Canada showing the location of the Archean Slave Province and Acasta Gneiss Complex (AGC). (b) Simplified geological map of the central portion of the AGC after Iizuka et al. (2007) and Reimink, Chacko, et al. (2016). Location of (c) is highlighted by red square. (c) Geological map of the Acasta discovery island after Reimink, Chacko, et al. (2016) showing the sample location.

et al., 1989; Bowring, Williams, & Compston, 1989), much emphasis has been placed on isotopic studies to refine their crystallization age and subsequent evolution (Reimink, Chacko, et al., 2016).

Zircon U–Pb ages determined on texturally-complex grains in several samples from the AGC record more than a billion years of magmatic activity and crustal reworking from 4.03 Ga to 2.9 Ga, with rare xenocrystic cores as old as 4.2 Ga (Iizuka et al., 2006). However, tectonic interlayering and mixing of different lithological components at a decametre- to centimetre-scale have made it difficult to derive unambiguous petrogenetic information about their igneous precursors (e.g., Mojzsis et al., 2014; Reimink et al., 2014). Subsequent mapping of field relationships and deformation between the various components that constitute the AGC has revealed two contrasting lithological domains, which are separated by a major northeast-trending fault (Iizuka et al., 2007; Figure 1b): (1) a western high-strain domain, where different lithologies are intimately intermingled, and (2) a low-strain eastern domain, which also encompasses the Idiwhaa tonalitic gneiss, in which individual rock units can be distinguished by their field, petrological, geochemical and geochronological characteristics (Reimink et al., 2014; Reimink, Chacko, et al., 2016).

In the eastern domain, several metamorphic events have been inferred at c. 3.75, c. 3.65, c. 3.60 and 3.4–3.2 Ga based on the U–Pb ages of zircon overgrowths (Kirkland et al., in review; Bowring & Williams, 1999; Iizuka et al., 2007; Reimink et al., 2014; Reimink, Chacko, et al., 2016; Stern & Bleeker, 1998). However, any evidence for the older events in the rock-forming mineral assemblages appears to have been overprinted by pervasive partial melting (migmatization) of the gneisses during the latest Archean event (Guitreau et al., 2014). Moorbath et al. (1997) argued for a pervasive high-grade metamorphic event at 3.37 ± 0.06 Ga that induced partial melting of the AGC gneisses and led to widescale resetting and open-system behaviour of Nd isotopes. Indeed, titanite from these rocks has yielded a Sm–Nd regression age of 3.09 ± 0.19 Ga (Fisher et al., 2020), and zircon records U–Pb ages of *c.* 3.2 Ga, supporting widespread resetting and modification of various isotopic systems in the AGC at that time. Subsequently, Ar–Ar data from hornblende and biotite (Hodges et al., 1995) and U–Pb data from apatite and titanite (Antoine et al., 2020; Davidek et al., 1997; Fisher et al., 2020; Sano et al., 1999) reveal that the AGC was affected by the 1.9–1.8 Ga Wopmay orogeny, which records the collision between the Slave craton and

15251314, 2024, 3, Downloaded from https://onlinelibrary.wiley.com/doi/10.1111/jmg.12759 by Universitat Bern, Wiley Online Library on [13/03/2024]. See the Terms and Conditions (https://onlinelibrary.wiley.com/terms-and-conditions) on Wiley Online Library for rules of use; OA articles are governed by the applicable Creative Commons License

Hottah Terrane (Hoffman & Bowring, 1984; Sano et al., 1999; St-Onge & Davis, 2018).

This study uses two samples of tonalitic gneiss (AC-12, AC-13) from the eastern low-strain domain collected by Prof. Stephen Moorbath in 1995 and generously provided to us by the University of Oxford. The approximate sample location, which is based on Moorbath's field description made before the widespread availability of GPS, is marked by the red star in Figure 1c.

3 | METHODS

3.1 | Mineral chemistry

Major element compositions of minerals were measured by a JEOL 8530F electron probe micro analyser (EPMA) at the University of Western Australia. A 15 keV accelerating voltage and a 20 nA current were used, with a beam size of 1 μm for garnet and feldspar, and a defocused beam size of 5 μm for biotite and amphibole. In addition, a 1 × 1 cm^2 area was analysed in each thin section using a JEOL JXA-8200 superprobe at the Institute of Geological Sciences at the University of Bern, following the analytical procedures described in Lanari and Piccoli (2020). Working conditions for area scans were: 15 keV accelerating voltage, 100 nA beam current and a step size of 10 μm, resulting in an image resolution of 1,000 × 1,000 pixels for the final quantitative compositional maps. Data reduction, including the production of phase maps and garnet major element profiles along representative transects, was produced in XMapTools 4 (Lanari et al., 2014, 2019).

3.2 | Bulk-rock chemistry and phase equilibrium modelling

Isochemical P–T phase diagrams (pseudosections) were calculated using Perple_X version 6.9.0 (Connolly, 1990, 2005, 2009) and the internally-consistent thermodynamic dataset version 6.2 (updated 6. February 2012) of Holland and Powell (2011). Both samples were modelled in the 10-component NCKFMASHTO compositional system (NaO_2–CaO–K_2O–FeO–MgO–Al_2O_3–SiO_2–TiO_2–O_2), utilizing activity-composition models for solid solution phases as follows: tonalitic melt, augite and clinoamphibole from Green et al. (2016); orthopyroxene, garnet, biotite and white mica from White et al. (2014); ternary feldspar from Holland and Powell (2003); epidote from Holland and Powell (2011); ilmenite (White et al., 2000, 2014); and magnetite (White et al., 2002). Pure phases include quartz, rutile, sillimanite, andalusite, kyanite and aqueous fluid (H_2O). The compositions used for phase equilibrium modelling were derived from the representative 1 cm^2 area in each thin section and calculated using XMapTools 4 (Lanari et al., 2014, 2019) as described above and using a density correction (Lanari & Engi, 2017). To account for the occurrence of apatite, calcium contents were proportionally corrected for the respective phosphorus content in each sample; no monazite was observed. Throughout, thermodynamic model-derived uncertainties are taken to be at least ± 50°C and ± 1 kbar (Palin, White, & Green, 2016; Powell & Holland, 2008).

The amount of H_2O used in phase diagram calculations was estimated using the measured abundance of biotite and amphibole in each sample, assuming these minerals contain 4 wt% and 2 wt% H_2O, respectively, then validated through the construction of isobaric T–H_2O sections calculated at a pressure estimated from preliminary P–T modelling for both samples ($P = 5.5$ kbar) over a range of water contents (0.01 wt%–2.00 wt% H_2O). These estimates are remarkably close to the amount of water needed to minimally saturate the solidus in H_2O at that pressure, assuming that any free fluid phase produced by subsolidus dehydration reactions was lost from the system, justifying the approach. Similarly, bulk-rock $X_{Fe^{3+}} = Fe^{3+}/(Fe^{2+} + Fe^{3+})$ ratios were estimated using isobaric ($P = 5.5$ kbar) T–$X_{Fe^{3+}}$ phase diagrams to compare the petrological effects of variable oxidation during metamorphism, ranging from highly reduced conditions ($X_{Fe^{3+}} = 0.05$) to more oxidized conditions ($X_{Fe^{3+}} = 0.20$). Compositions used for phase equilibrium modelling are given in Table 1. Mineral abbreviations follow Warr (2021), plus 'Wm' for white mica.

3.3 | In situ garnet Lu–Hf geochronology

Due to the low modal abundance of garnet in both samples (< 3 vol.%), garnet was handpicked from grain separates and mounted in epoxy to maximize the quantity of material available for analysis. Grain mounts were ground using 2000 grit sandpaper and subsequently polished with 9 μm, 3 μm and 1 μm diamond paste. Prior to analysis, garnet was imaged in back-scattered electron mode under a scanning electron microscope to guide the location of analytical spots.

Garnet Lu–Hf analysis used laser-ablation tandem inductively coupled plasma mass spectrometry (LA–ICP–MS/MS) at the John de Laeter Centre (JdLC) at Curtin University, Australia. Data were acquired in one analytical session using a RESOlution 193 nm excimer laser-ablation system connected to an Agilent 8900 QQQ ICP-MS. Analytical procedures closely follow those

15251314, 2024, 3, Downloaded from https://onlinelibrary.wiley.com/doi/10.1111/jmg.12759 by Universitat Bern, Wiley Online Library on [13/03/2024]. See the Terms and Conditions (https://onlinelibrary.wiley.com/terms-and-conditions) on Wiley Online Library for rules of use; OA articles are governed by the applicable Creative Commons License

TABLE 1 Bulk-rock compositions (Mol.%) used for phase equilibrium modelling.

Sample	Pseudo-section	SiO_2	TiO_2	Al_2O_3	MgO	FeO^{tot}	CaO	Na_2O	K_2O	H_2O	O
AC-13	P–T	75.958	0.443	7.861	5.722	0.867	3.274	2.959	1.008	1.908	0.143
	T–X_{H_2O} (X_0)	77.407	0.452	8.011	5.831	0.884	3.336	3.016	1.027	0.036	0.146
	T–X_{H_2O} (X_1)	72.161	0.421	7.468	5.436	0.824	3.110	2.811	0.958	6.811	0.136
	T–$X_{Fe^{3+}}$ (X_0)	75.958	0.443	7.861	5.722	0.867	3.274	2.959	1.008	1.908	0.072
	T–$X_{Fe^{3+}}$ (X_1)	75.958	0.443	7.861	5.722	0.867	3.274	2.959	1.008	1.908	0.286
AC-12	P–T	75.441	0.452	7.646	5.736	1.915	2.408	2.897	1.116	2.388	0.143
	T–X_{H_2O} (X_0)	77.259	0.463	7.830	5.875	1.962	2.466	2.967	1.143	0.036	0.147
	T–X_{H_2O} (X_1)	72.001	0.432	7.297	5.475	1.828	2.299	2.765	1.065	6.839	0.137
	T–$X_{Fe^{3+}}$ (X_0)	75.441	0.452	7.646	5.736	1.915	2.408	2.897	1.116	2.388	0.072
	T–$X_{Fe^{3+}}$ (X_1)	75.441	0.452	7.646	5.736	1.915	2.408	2.897	1.116	2.388	0.287

Note: Total iron is expressed as FeO^{tot}. The amount of ferric iron is expressed as O (oxygen), which is equivalent to the amount of Fe_2O_3 based on the following equation: $Fe_2O_3 = 2 \times FeO + O$.

described by Simpson et al. (2021). Laser fluence was ~2.5 J/cm^2 and the ablation spot diameter was set to 130 μm with a repetition rate of 10 Hz to ensure reasonable sensitivity for low Hf concentrations. A mixture of 20% NH_3 and 80% He was used as the reaction gas in the collision cell to remove isobaric interferences of Lu and Yb on ^{176}Hf. Analysed isotopes include those needed for Lu–Hf geochronology as well as those used to monitor mineral inclusions in garnet that may affect the measured isotopic ratios (Simpson et al., 2021). The following masses were measured sequentially (dwell time in ms); ^{27}Al (5), ^{43}Ca (5), ^{47}Ti (5), ^{89}Y (5), ^{90}Zr (5), ^{140}Ce (5), ^{172}Yb (10), $^{172+82}$Yb (30), ^{175}Lu (10), $^{175+16}$Lu (20), $^{175+82}$Lu (100), $^{176+82}$Hf (100), $^{178+82}$Hf (100). ^{175}Lu was measured as a proxy for ^{176}Lu, and ^{178}Hf was measured as a proxy for ^{177}Hf. Present-day ^{176}Lu/^{175}Lu (0.02659) and ^{177}Hf/^{178}Hf ratios (0.682) were assumed (De Biévre & Taylor, 1993). Data reduction was performed in Iolite4 (Paton et al., 2011; and references therein), correcting for background signal, mass bias and instrument drift for ^{176}Lu/^{177}Hf and ^{176}Hf/^{177}Hf ratios. Analyses that were clearly affected by other Lu- or Hf-bearing accessory phases (e.g., zircon, allanite, apatite, titanite) were excluded during subsequent data evaluation.

Analyses used NIST 610 glass as the primary reference material (^{176}Lu/^{177}Hf $= 0.1379 \pm 0.005$ and ^{176}Hf/^{177}Hf $= 0.282111 \pm 0.000009$; Nebel et al., 2009; all errors in 2sd) to correct for analytical drift, which was analysed after every 18 unknowns. Following this procedure, NIST 612 gave weighted mean ^{176}Lu/^{177}Hf and ^{176}Hf/^{177}Hf ratios of 0.1345 ± 0.0015 ($n = 25$, MSWD $= 4.34$) and 0.2815 ± 0.0046 ($n = 24/25$; MSWD $= 2.14$), respectively, consistent with published values (Nebel et al., 2009). Garnet from the Högsbo pegmatite (Gothenburg, Sweden) was used as a secondary standard to correct for the effects of matrix-induced elemental fractionation, producing an age of 1064 ± 6 Ma ($n = 36$, MSWD $= 2.1$) compared to the published U–Pb columbite crystallization age of 1029 ± 1.7 Ma (Romer & Smeds, 1996). This offset towards an older age for laser-ablation Lu–Hf dating of Högsbo garnet is consistent with previous analysis from other labs (e.g., Brown et al., 2022; Simpson et al., 2021) and has been taken into account for all unknowns by correcting the ^{176}Lu/^{176}Hf ratios by the discrepancy between the published columbite and measured Lu–Hf garnet age (~3.3%).

Lu–Hf garnet ages were calculated in IsoplotR (Vermeesch, 2018) using inverse isochron regression to minimize strong error correlations between ^{176}Lu/^{177}Hf and ^{176}Hf/^{177}Hf that may obscure data dispersion related to geological complexity when plotted in the conventional isochron diagram (Li & Vermeesch, 2021). Isochrons were anchored to an upper intercept of ^{177}Lu/^{176}Hf $= 0.0001 \pm 0.0001$ and ^{177}Hf/^{176}Hf $= 3.546 \pm 0.050$ to ensure they return reasonable initial Hf compositions (^{176}Hf/^{177}Hf)$_0$ that fall within the range of reported terrestrial values (Simpson et al., 2021, 2023). Individual data uncertainties are 2σ with resulting age uncertainties shown as 95% confidence intervals without the $\sqrt{\text{MSWD}}$ overdispersion multiplier (Vermeesch, 2018).

3.4 | Garnet trace element analysis

Laser-ablation inductively coupled plasma mass spectrometry (LA–ICP–MS) data collection for determination of trace element (TE) concentrations in garnet was conducted at the JdLC, Curtin University, Australia. Data were acquired from all garnet grains analysed previously for Lu–Hf isotopes and along representative line profiles

15251314, 2024, 3, Downloaded from https://onlinelibrary.wiley.com/doi/10.1111/jmg.12759 by Universitat Bern, Wiley Online Library on [13/03/2024]. See the Terms and Conditions (https://onlinelibrary.wiley.com/terms-and-conditions) on Wiley Online Library for rules of use; OA articles are governed by the applicable Creative Commons License

across the best-preserved garnet grain in each sample. Where possible, TE analysis spots were positioned close to existing ablation pits of Lu–Hf analyses to sample the same compositional domain in garnet, whereas TE line profiles followed those of corresponding major element transects. Data were acquired in one analytical session using a RESOlution 193 nm excimer laser-ablation system connected to an Agilent 8900 QQQ ICP–MS. Garnet TE concentrations were determined using an ablation spot size of 33 μm, with a laser fluence of 2.0 J/cm^2 and 10 Hz repetition rate. The following nuclides were measured sequentially (dwell time 20 ms each); ^{7}Li, ^{9}Be, ^{23}Na, ^{24}Mg, ^{27}Al, ^{29}Si, ^{39}K, ^{43}Ca, ^{45}Sc, ^{49}Ti, ^{51}V, ^{52}Cr, ^{55}Mn, ^{57}Fe, ^{59}Co, ^{60}Ni, ^{63}Cu, ^{66}Zn, ^{85}Rb, ^{88}Sr, ^{89}Y, ^{91}Zr, ^{93}Nb, ^{95}Mo, ^{133}Cs, ^{137}Ba, ^{193}La, ^{140}Ce, ^{141}Pr, ^{146}Nd, ^{147}Sm, ^{153}Eu, ^{157}Gd, ^{159}Tb, ^{163}Dy, ^{165}Ho, ^{166}Er, ^{169}Tm, ^{172}Yb, ^{175}Lu, ^{178}Hf, ^{181}Ta, ^{182}W, ^{201}Hg, ^{208}Pb, ^{232}Th, ^{238}U.

The reference materials used were NIST 610, NIST 612 and GSD-1G which were analysed after every 15 unknows. Data reduction was undertaken in Iolite 4 (Paton et al., 2011; and references therein), utilizing NIST 612 as the primary reference material and ^{29}Si as the internal reference standard with an average concentration of ~17 wt% Si in garnet. Calculations for limits of detection (LOD) follow those of Howell et al. (2013). Ablation signals were monitored for anomalies resulting from contamination by micro-inclusions (mainly zircon, titanite and allanite), as evident by distinct ablation spikes in Ti, Zr, light and middle rare earth elements and/or Hf. Of 139 total trace element analyses, 21 were eliminated during data reduction. Analytical performance was assessed by comparing secondary standards to their published reference values (GeoREM database; Jochum et al., 2005). Accuracy for NIST 610 was <5% for all elements except Be (−6%), Mg (20%) and Ti (11%), and for GSD-1G < 15% except for Be (−19%), Y and Gd (both −16%).

4 | RESULTS

4.1 | Petrography and mineral chemistry

4.1.1 | AC-13

Sample AC-13 is a layered tonalitic gneiss composed of quartz (~42 vol.%), plagioclase (~39 vol.%), biotite (~8 vol.%), amphibole (~8 vol.%) and garnet (~3 vol.%) with accessory magnetite, ilmenite, apatite, allanite and zircon (Figure 2a; abundances based on phase maps produced in XMapTools). Alternating quartzofeldspathic and garnet–hornblende-bearing layers define a fine gneissic banding, along with a foliation defined by the preferred alignment of hornblende and biotite (Figure 2c). Garnet typically occurs as rounded or slightly elongated anhedral blasts (1–3 mm; Figure 2e), of which some are pervasively fractured and partially replaced by plagioclase and biotite with or without epidote and hornblende. Rounded and tabular inclusions of quartz, plagioclase and hornblende are rare and show no clear alignment. Garnet shows flat compositional profiles through the core and rim within well-preserved blasts and is typically almandine-rich with very low pyrope contents (Figure 3a, c). Compositions range from $X_{\mathrm{alm}} = 0.59$ to 0.72, $X_{\mathrm{grs}} = 0.09$ to 0.25, $X_{\mathrm{sps}} = 0.06$ to 0.13 and $X_{\mathrm{prp}} = 0.01$ to 0.04. Where present, zoning is restricted to a few microns at resorbed grain margins, close to fractures or in the vicinity of mineral inclusions, and shows a sharp rimward decrease in almandine and pyrope and an increase in spessartine and grossular contents, respectively, consistent with post-peak diffusion and retrogressive uptake of Mn during resorption (Kelly et al., 2011; Spear, 1995). In garnet, X_{Mg} (atomic Mg/[Mg + Fe^{2+}]) varies between 0.02 and 0.05.

Amphibole is strongly pleochroic, ranging from khaki green to a dark blue-green, and typically occurs either as elongate grains with biotite in discontinuous mafic foliae or as rare anhedral porphyroblasts (up to 2 mm; Figure 2a). Following the classification of Hawthorne et al. (2012), amphibole compositions (based on 23 O) range from pargasite to sadanagaite with Si = 5.98–6.10 apfu, $^{\mathrm{A}}$(Na + K + 2Ca) = 0.53–0.67, $^{\mathrm{C}}$(Al + Fe^{3+} + 2Ti) = 1.42–1.64 and $X_{\mathrm{Mg}} = 0.11$–0.22. No significant zoning of individual crystals was observed. Microlithons are dominated by recrystallized quartz bands and tabular to rounded plagioclase (1–2 mm) with interspersed fine-grained biotite and minor amphibole. We interpret rare quartzofeldspathic segregations as leucosomes and evidence for the former presence of melt. Plagioclase is weakly zoned with $X_{\mathrm{alb}} = 0.69$–0.76 increasing from core to rim. Biotite is Fe-rich ($X_{\mathrm{Mg}} = 0.12$–0.18) and has Al = 1.43–1.48 apfu and Ti = 0.20–0.25 apfu (based on 11 O). Partial retrogression of plagioclase to sericite is ubiquitous.

4.1.2 | AC-12

Sample AC-12 is a foliated tonalitic gneiss comprising quartz (~39 vol.%), plagioclase (~35 vol.%), K-feldspar (~5 vol.%), biotite (~14 vol.%), amphibole (~6 vol.%) and garnet (< 1 vol%) with accessory ilmenite, apatite, zircon and minor sulphides (Figure 2b). Compositional layering is much less clear in sample AC-12 than in sample AC-13, and sample AC-12 exhibits a higher degree of retrograde alteration. Garnet in sample AC-12 typically occurs as clusters of small anhedral fragments (< 100 μm)

15251314, 2024, 3, Downloaded from https://onlinelibrary.wiley.com/doi/10.1111/jmg.12759 by Universitat Bern, Wiley Online Library on [13/03/2024]. See the Terms and Conditions (https://onlinelibrary.wiley.com/terms-and-conditions) on Wiley Online Library for rules of use; OA articles are governed by the applicable Creative Commons License

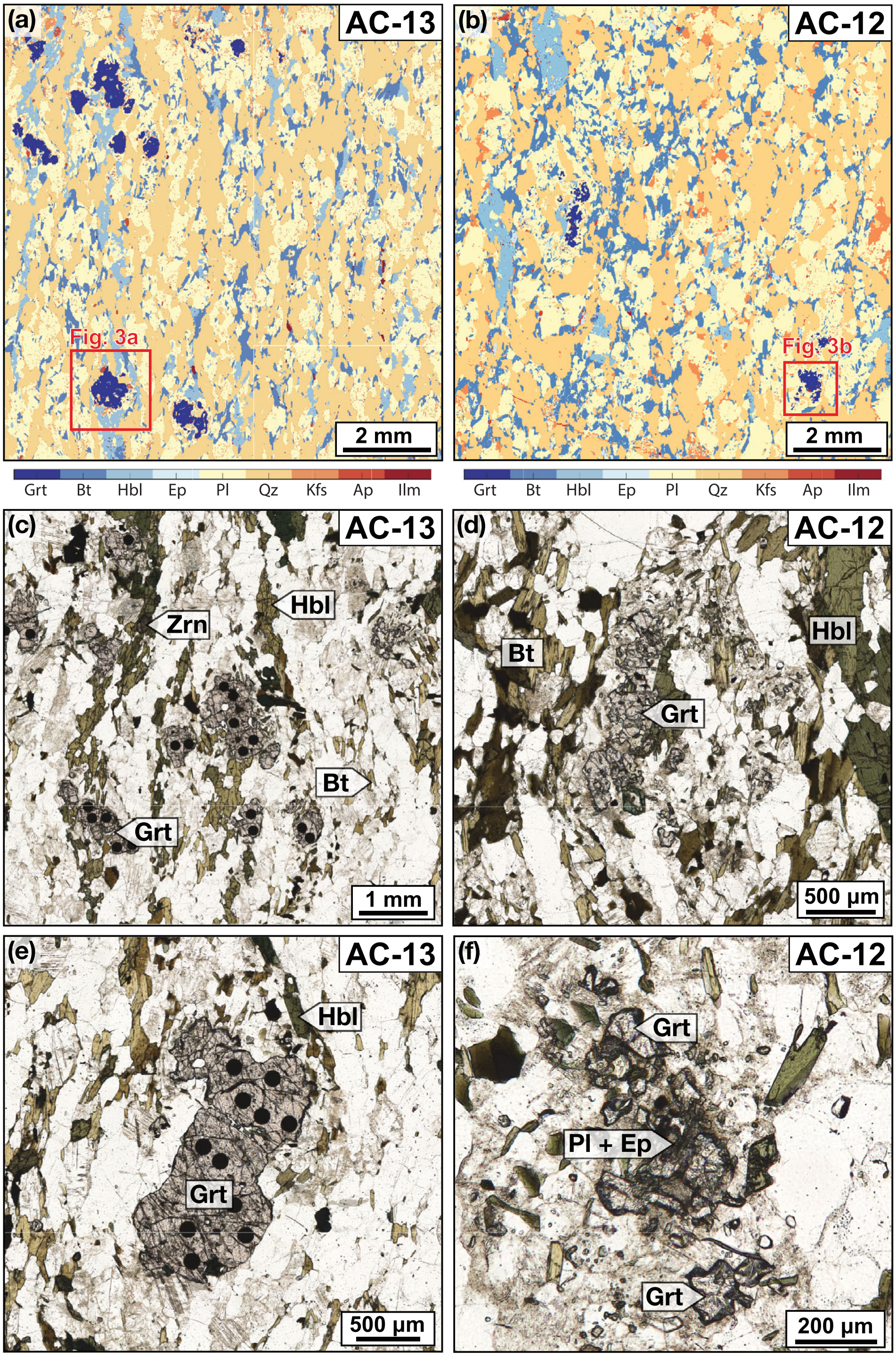

FIGURE 2 Phase maps (a–b) and petrographic microphotographs of representative garnet grains in sample AC-13 (c, e) and AC-12 (d, f) in plane-polarized light. (a) Phase map of a 1 × 1 cm^2 area used to deduce a local bulk composition for phase equilibrium modelling for sample AC-13 and (b) AC-12. Location of garnets used for compositional mapping and profiles are marked by red squares. (c) Overview of a garnet-hornblende-bearing layer with abundant anhedral, but still intact garnet grains. Breakdown/resorption of garnet (top right) is observed far less than in sample AC-12. Black circles in garnet correspond to laser-ablation pits of previous Lu–Hf analyses. (d) Strongly resorbed and fragmented garnet grain surrounded by dusty plagioclase, fine-grained epidote and biotite. Note the higher degree of retrograde alteration in this sample as indicated by the progressive breakdown of garnet and abundant overgrowth of biotite on hornblende. (e) Close-up of a large pervasively fractured garnet porphyroblast. (f) Close-up of the breakdown of garnet to plagioclase, epidote and minor biotite.

together with plagioclase and epidote that surround larger remnants of highly resorbed and fractured garnet grains (~1 mm; Figure 2d, f). Compositional maps and profiles reveal that larger garnet grains typically display patchy zoning, preserving portions that apparently escaped later re-equilibration (Figure 3b, c). These patches display higher almandine ($X_{alm} = 0.61–0.63$) and lower grossular contents ($X_{grs} = 0.15–0.24$) compared to the surrounding domains. Garnet affected by later re-equilibration has $X_{alm} = 0.47–0.50$, $X_{prp} = 0.01$, $X_{grs} = 0.28–0.36$ and $X_{sps} = 0.14–0.15$. The X_{Mg} of garnet is constant and varies from 0.02 to 0.03.

Amphibole forms ~0.5 mm long anhedral laths in close association with biotite within discontinuous layers, but also occurs as fine-grained crystals dispersed throughout the matrix (Figure 2b). Larger subhedral blasts (2–3 mm) are less common and contain rounded inclusions of quartz and plagioclase. Amphibole is of pargasite–

15251314, 2024, 3, Downloaded from https://onlinelibrary.wiley.com/doi/10.1111/jmg.12759 by Universitat Bern, Wiley Online Library on [13/03/2024]. See the Terms and Conditions (https://onlinelibrary.wiley.com/terms-and-conditions) on Wiley Online Library for rules of use; OA articles are governed by the applicable Creative Commons License

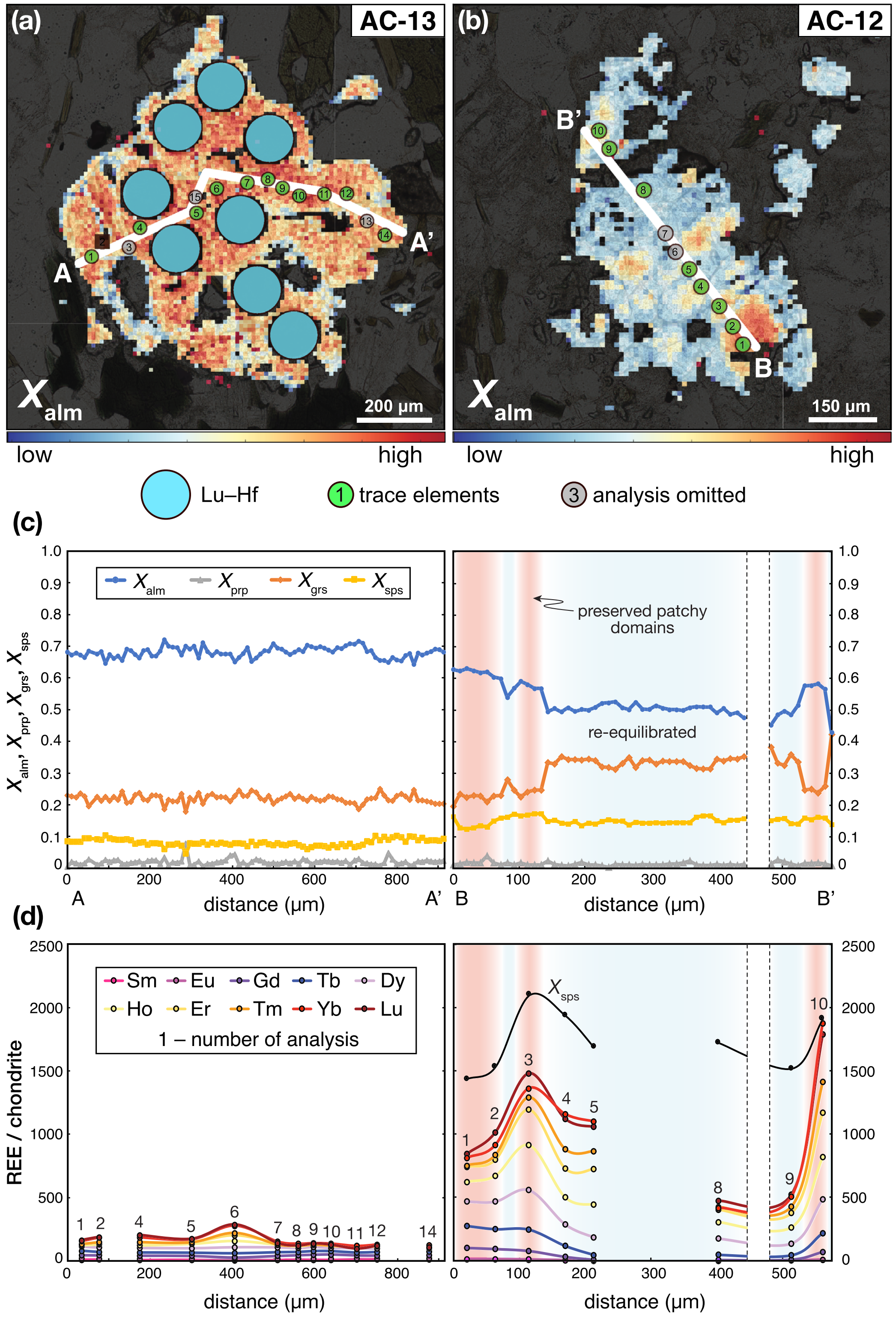

FIGURE 3 Maps of X_{alm} in garnet (a–b) and associated major and trace element compositional profiles (c–d). Garnet in sample AC-13 generally has high X_{alm} and shows flat major element compositional profiles through the core and rim, with relative enrichment of HREE and depletion of LREE in the core. In contrast, garnet in sample AC-12 shows patchy zoning in major elements (mainly X_{alm} and X_{grs}) and a significantly higher HREE budget throughout the entire grain compared to garnet in AC-13. Variations in trace element concentrations do not mimic the patchy zoning observed in major elements but rather follow the trend defined by X_{sps}. The colour scale of compositional maps was adjusted individually for each sample to highlight zoning patterns. Spot analyses showing evidence for contamination by micro-inclusions were omitted in the trace element profiles and REE lighter than Sm are not shown due to their very low concentrations.

15251314, 2024, 3, Downloaded from https://onlinelibrary.wiley.com/doi/10.1111/jmg.12759 by Universitat Bern, Wiley Online Library on [13/03/2024]. See the Terms and Conditions (https://onlinelibrary.wiley.com/terms-and-conditions) on Wiley Online Library for rules of use; OA articles are governed by the applicable Creative Commons License

sadanagaite composition, with Si = 5.91–6.05 apfu, ^{A}(Na + K + 2Ca) = 0.67–0.71, ^{C}(Al + Fe^{3+} + 2Ti) = 1.44–1.60 and X_{Mg} = 0.21–0.23. Equigranular quartz and plagioclase (X_{alb} = 0.72) occur in the matrix in subequal proportions along with biotite and minor alkali-feldspar (X_{Or} = 0.91–0.97). Fine-grained plagioclase around garnet is generally more Ca-rich (X_{alb} = 0.66–0.67) and biotite (X_{Mg} = 0.25–0.26) is more magnesian than in sample AC-13, with Al = 1.49–1.53 apfu and Ti = 0.18–0.20 apfu. Late-stage sericitization of plagioclase and chloritization of biotite are widespread.

4.1.3 | Garnet trace elements

Rare earth element (REE) contents in garnet were determined for grains that were also analysed for Lu–Hf isotopes. In both samples, plots of chondrite-normalized REE abundances (chondrite values from Boynton, 1984) for garnet show steep light rare earth element (LREE)-depleted to heavy rare earth element (HREE)-enriched patterns with no prominent Eu anomalies (Figure 4). The normalized REE values generally range from 10^{-2} to 10^{3}, with most of the LREE values reflecting abundances close to or below detection limits. Garnets from sample AC-12 exhibit on average lower middle and higher heavy REE abundances compared to AC-13, and display a much wider spread in normalized REE patterns in general (Figure 4). This is particularly evident for some middle REEs (i.e., Sm, Eu and Gd) whose concentrations span up to two orders of magnitude in AC-12.

Representative garnet grains selected for major element profiling were also analysed for trace elements (Figure 3d). For garnet in sample AC-13, line transects record mostly flat REE zoning with subtle Y + HREE enrichments in the core relative to the rim (e.g., core/rim ~2.2 for Lu and ~1.3 for Y), consistent with the incorporation of these elements into cores due to Rayleigh fractionation (e.g., Kohn, 2009), and either no variation in the LREE or slightly increasing concentrations towards the rim (e.g., core/rim ~0.4 for Sm). By contrast, REE abundances across garnet grains in sample AC-12 display a much higher variability and show no systematic variation between core and rim. Although limited by the spatial resolution of analyses, local enrichments in Y + HREE mimic the general trend of X_{sps}, but show no correlation with the patchy zoning observed in X_{alm} and X_{grs} (Figure 3d). The full dataset including reference materials and unknowns is detailed in the supplementary materials S1.

4.1.4 | Phase equilibrium modelling

The *P–T* pseudosections for the tonalitic gneiss samples were constructed from 550 to 900°C and 2 to 10 kbar. In both samples, quartz, plagioclase and ilmenite are stable throughout the modelled *P–T* window and have been omitted from the labelled fields for clarity. The stability of other selected key minerals (i.e., garnet, hornblende, biotite and K-feldspar) is indicated by the coloured lines.

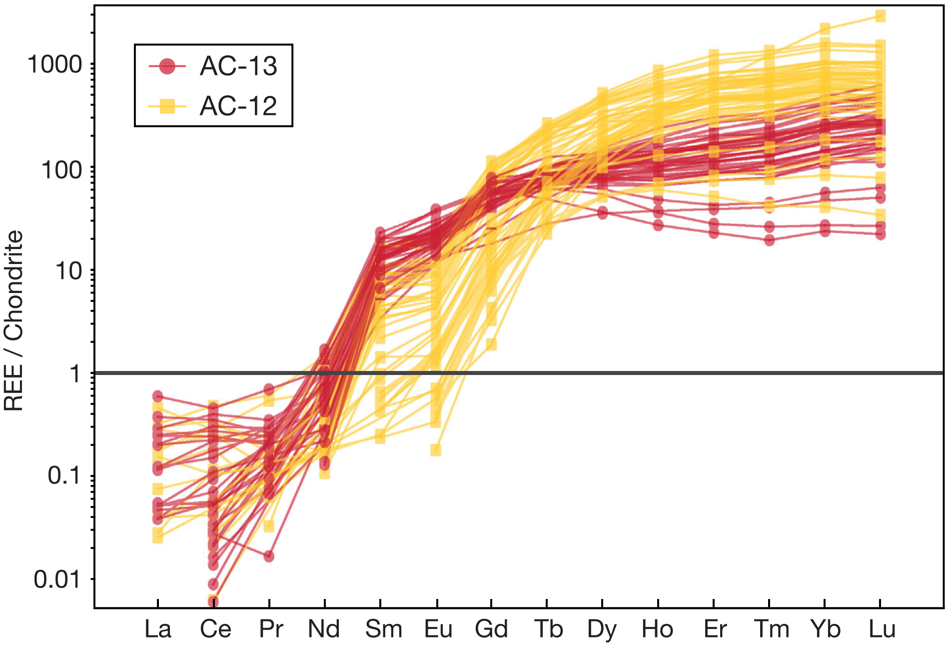

FIGURE 4 Chondrite-normalized REE patterns for garnet grains analysed for Lu–Hf dating from samples AC-13 and AC-12. Chondrite values from Boynton (1984).

15251314, 2024, 3, Downloaded from https://onlinelibrary.wiley.com/doi/10.1111/jmg.12759 by Universitat Bern, Wiley Online Library on [13/03/2024]. See the Terms and Conditions (https://onlinelibrary.wiley.com/terms-and-conditions) on Wiley Online Library for rules of use; OA articles are governed by the applicable Creative Commons License

4.1.5 | AC-13

Phase equilibrium modelling predicts the observed mineral assemblage Qz + Pl + Bt + Hbl + Grt + Ilm + Mag to be stable above the H_2O-saturated (wet) solidus at 675–800°C and 4.5–7.0 kbar. The assemblage is constrained to a relatively narrow field that is bound towards lower pressures and temperatures by the absence of garnet, at higher pressures by the absence of hornblende, and at higher temperatures by the presence of orthopyroxene and K-feldspar, which are not observed in the sample (Figure 5a).

Metamorphic peak conditions were further constrained by comparing the observed and calculated modal proportions of the rock-forming minerals. This approach may be particularly useful for high-grade rocks, where evidence for prograde and peak compositional zoning may have been erased due to diffusive relaxation or later re-equilibration, making *P*–*T* estimates based on compositional constraints less reliable (e.g., Spear, 1995). To better constrain *P*–*T* conditions, isopleths for the observed modes of garnet, amphibole and biotite in sample AC-13 were plotted for the interpreted metamorphic peak phase assemblage and adjoining fields (Figure 5b). We assign an arbitrary uncertainty of ±1 vol.% to garnet modes and ±2 vol.% to those for biotite and hornblende to account for sample heterogeneity and any potential retrograde overprint. For sample AC-13, the intersection of garnet and biotite modal isopleths occurs within the stability field of the observed phase assemblage, which constrains metamorphic peak conditions to 750–780°C and 4.5–5.4 kbar (black polygon in Figure 5b). Although the modal isopleths for hornblende plot just outside the peak field within uncertainty, the calculated abundance of most phases matches petrographic observations well, as shown in Figure 6.

Several studies have demonstrated that, among other variables, mineral modes and compositions are significantly affected by bulk-rock H_2O content and oxidation (expressed here as $X_{Fe^{3+}}$) of the modelled composition (Diener & Powell, 2010; Guiraud et al., 2001; Lanari & Duesterhoeft, 2019; Palin, White, & Green, 2016). We investigate the impact of these variables on the observed peak phase assemblage and stability of key minerals

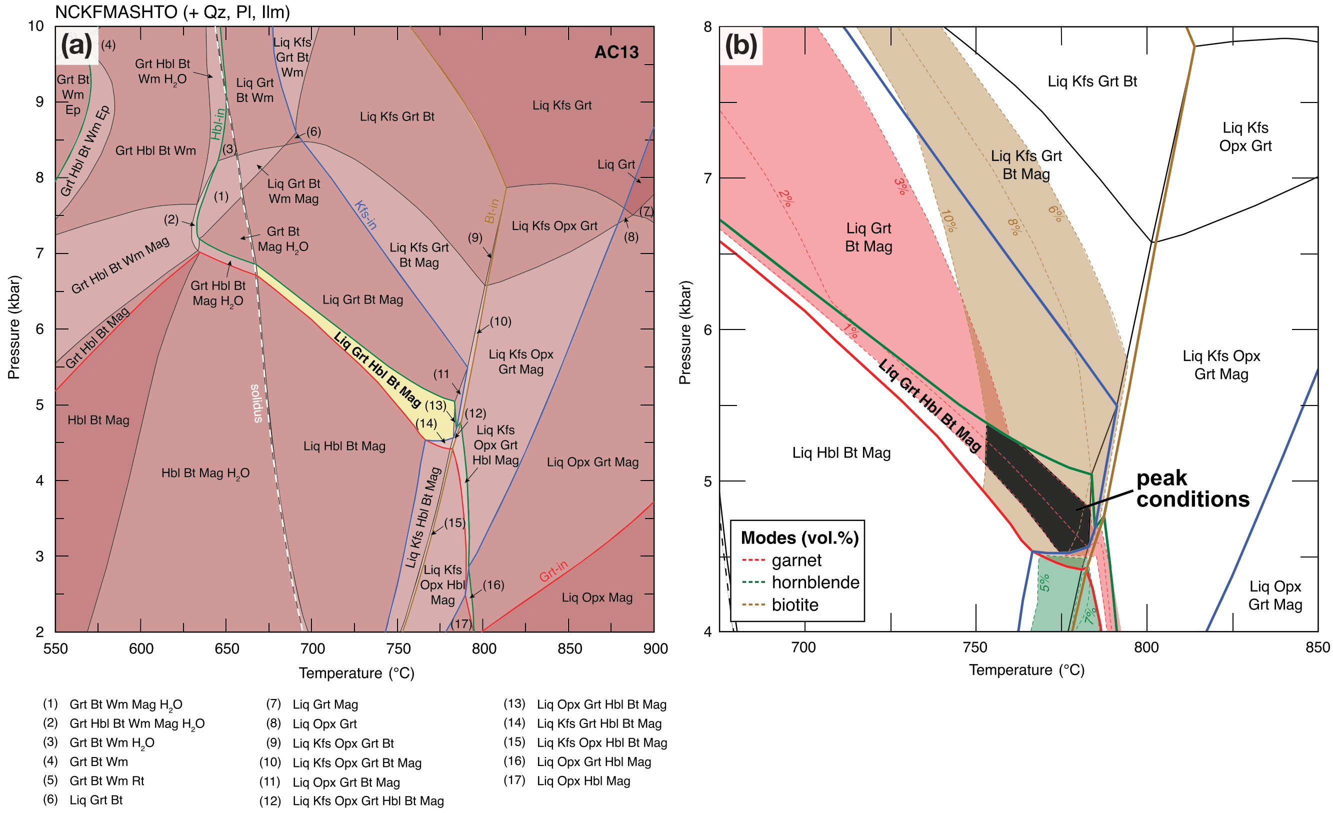

FIGURE 5 (a) *P*–*T* pseudosection for sample AC-13. The observed mineral assemblage is marked by the yellow field. The stability of key minerals is indicated by coloured curves: red – garnet, blue – K-feldspar, green – hornblende, brown – biotite, white dashed – solidus. (b) Close-up of the peak field contoured for the observed modes of garnet, hornblende and biotite with an arbitrary uncertainty envelope of ±1 vol.% for garnet and ±2 vol.% for hornblende and biotite. The intersection of garnet and biotite modal isopleths constrain the metamorphic peak conditions to 750–780°C and 4.5–5.4 kbar.

15251314, 2024, 3, Downloaded from https://onlinelibrary.wiley.com/doi/10.1111/jmg.12759 by Universitat Bern, Wiley Online Library on [13/03/2024]. See the Terms and Conditions (https://onlinelibrary.wiley.com/terms-and-conditions) on Wiley Online Library for rules of use; OA articles are governed by the applicable Creative Commons License

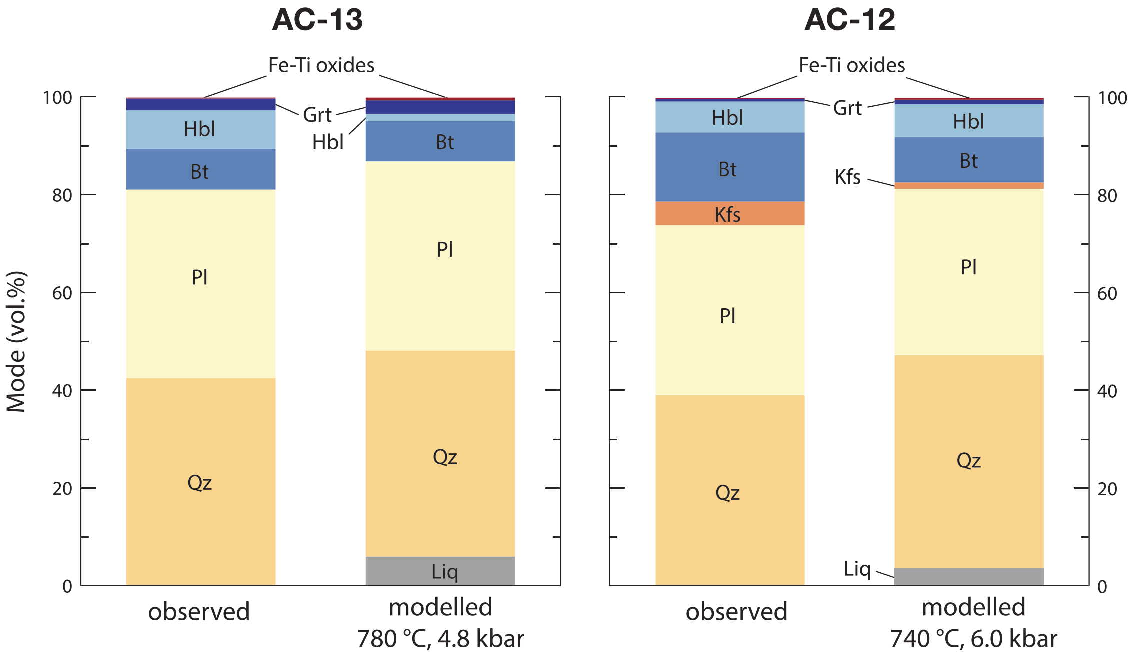

FIGURE 6 Comparison of the observed and modelled phase proportions of tonalitic gneisses at the predicted metamorphic peak conditions.

using isobaric T–H_2O and T–$X_{Fe^{3+}}$ pseudosections constructed at $P = 5.5$ kbar (Figure 7). The bulk-rock H_2O content and $X_{Fe^{3+}}$ used for the construction of P–T pseudosections (Figure 5) are indicated by the vertical dashed lines, and all endmember bulk-rock compositions are reported in Table 1.

Figure 7a demonstrates how lowering bulk-rock water contents increases the temperature of the (H_2O-undersaturated) solidus, and hence lowers melt fertility. This is particularly evident for the transition from fluid-undersaturated to (subsolidus) fluid-saturated compositions, where solidus temperatures drop by more than 100°C (from ~790°C to 675°C). Several lines of evidence indicate that the observed phase assemblage of sample AC-13 is best reproduced by modelling a subsolidus H_2O-saturated bulk composition. In particular, hornblende is only stable in compositions that are saturated (or almost saturated) in H_2O, constraining the minimum bulk-rock water content to ~0.40 wt% H_2O. In addition, K-feldspar is absent in sample AC-13 and is predicted to be stable only in fluid-undersaturated bulk compositions. Garnet stability in subsolidus phase assemblages is restricted to fluid-undersaturated bulk compositions (H_2O < 0.5 wt%), but is largely unaffected by increasing bulk-rock H_2O at suprasolidus conditions. The absence of magnetite from the interpreted peak assemblage constrains the bulk-rock water content of sample AC-13 to a maximum of ~1.6 wt % H_2O (for $X_{Fe^{3+}} = 0.1$), although magnetite stability is strongly affected by redox conditions (Figure 7a).

The effects of varying bulk-rock oxidation are shown in Figure 7b, in which $X_{Fe^{3+}}$ ranges from highly reduced ($X_{Fe^{3+}} = 0.05$) to more oxidized conditions ($X_{Fe^{3+}} = 0.20$). The stability of the observed phase assemblage is largely unaffected by variations in $X_{Fe^{3+}}$ within the modelled range. The interpreted peak field is confined to a temperature interval ranging from ~720 to 760°C by the coexistence of garnet and hornblende and becomes progressively narrower for increasing $X_{Fe^{3+}}$. The appearance of garnet in subsolidus phase assemblages (at $P = 5.5$ kbar) is restricted to relatively reduced bulk-rock compositions ($X_{Fe^{3+}} < 0.11$), whereas its stability at suprasolidus conditions is largely insensitive to varying $X_{Fe^{3+}}$. Ilmenite as the dominant Fe–Ti-oxide within sample AC-13 is stable over the entire T–$X_{Fe^{3+}}$ range considered here and coexists with magnetite in bulk-rock compositions with $X_{Fe^{3+}} > 0.08$ (Figure 7b). Magnetite-absent assemblages below ~850°C are restricted to very reduced compositions, which fail to reproduce the observed mineral assemblage.

4.1.6 | AC-12

The P–T pseudosection for sample AC-12 closely resembles that for sample AC-13 (Figure 8a). Notable differences include the extended stability of K-feldspar towards lower temperatures, the occurrence of aluminosilicates in some phase assemblages below 725°C and the absence of

15251314, 2024, 3, Downloaded from https://onlinelibrary.wiley.com/doi/10.1111/jmg.12759 by Universitat Bern, Wiley Online Library on [13/03/2024]. See the Terms and Conditions (https://onlinelibrary.wiley.com/terms-and-conditions) on Wiley Online Library for rules of use; OA articles are governed by the applicable Creative Commons License

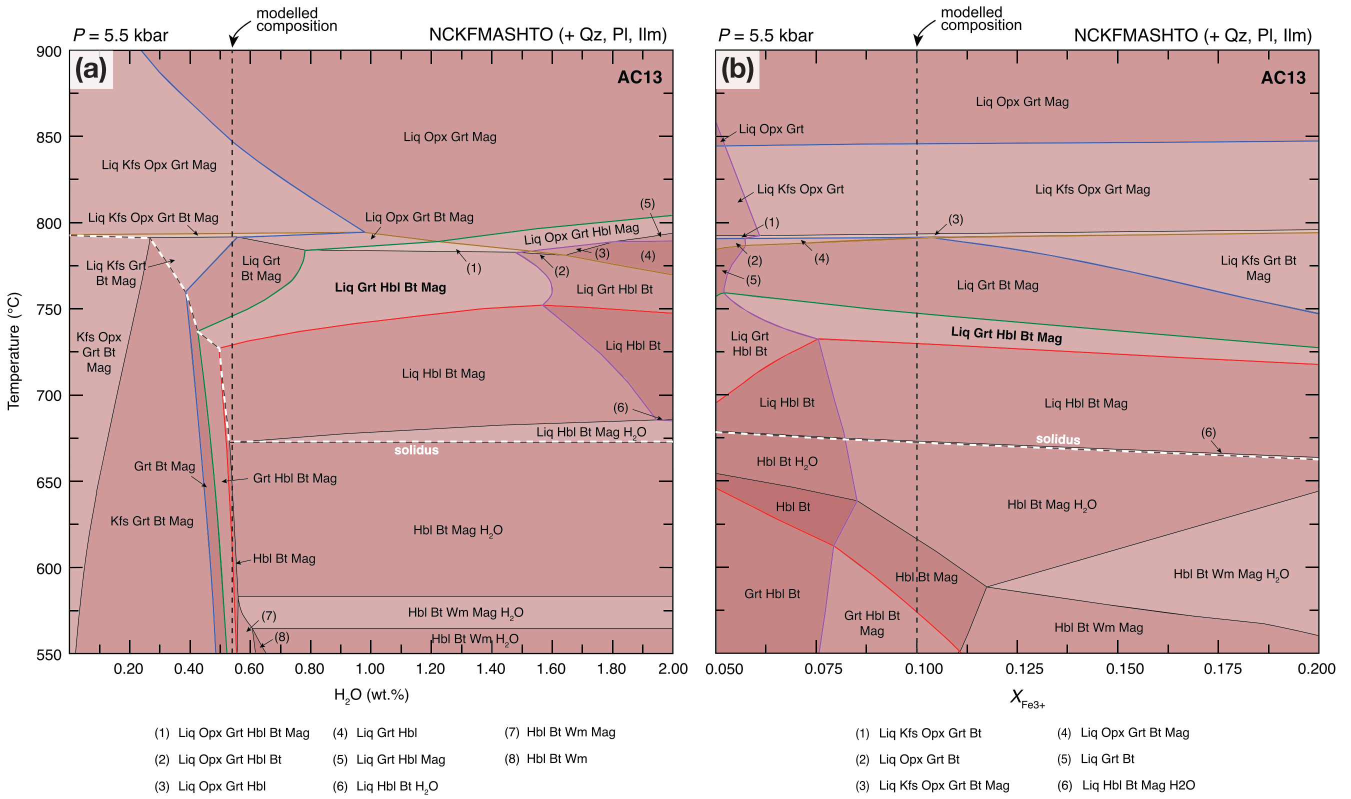

FIGURE 7 (a) T–H_2O and (b) T–$X_{Fe^{3+}}$ pseudosection for sample AC-13 showing the effects of varying bulk-rock water contents and oxidation state on the stability of modelled phase assemblages. Composition used for the construction of the P–T pseudosection is indicated by the vertical dashed line. The observed peak phase assemblage is highlighted in bold. Coloured curves mark the stability of key minerals: red – garnet, blue – K-feldspar, green – hornblende, brown – biotite, magenta – magnetite, white dashed – solidus.

magnetite in all phase assemblages at temperatures below ~700–800°C and pressures below ~8 kbar. The observed mineral assemblage comprising Qz + Pl + Kfs + Bt + Hbl + Grt + Ilm is predicted to be stable above the wet solidus at conditions of $T = 725$–$825°C$ and $P = 5.0$–7.0 kbar. This phase assemblage field is bound by the absence of K-feldspar towards lower temperatures and the appearance of orthopyroxene towards higher temperatures. Estimates of the peak pressure interval are mainly dictated by the absence of garnet below ~5.0 kbar and the appearance of magnetite above ~6.5 kbar in the temperature range of interest. Similar to sample AC-13, metamorphic peak conditions were further constrained by the intersection of modal isopleths of garnet and hornblende within the stability field of the observed peak assemblage to 725–775°C and 5.7–6.2 kbar (black polygon in Figure 8b). Overall, the predicted modal proportions of most phases are in good agreement with those observed (Figure 6). Although the amount of biotite observed in the thin section exceeds that predicted by phase equilibrium modelling at the inferred peak metamorphic conditions, it is consistent with the pronounced retrograde replacement of garnet and hornblende by biotite in this sample.

Isobaric T–X phase diagrams used to investigate the petrological effects of varying bulk-rock H_2O contents and oxidation are shown in Figure 9. Phase relationships and stabilities are generally similar to those observed in sample AC-13. Minor differences in the observed mineral assemblage include the extended stability of K-feldspar towards higher bulk-rock H_2O contents over a large temperature interval at suprasolidus conditions and the lack of magnetite in all fluid-saturated compositions below ~825°C (Figure 9a). Garnet stability at subsolidus conditions is restricted to fluid-undersaturated compositions and approximately coincides with the appearance of hornblende towards higher water contents. Biotite is stable in phase assemblages below ~800°C and is mostly insensitive to changes in bulk-rock H_2O content.

Initial estimates for the bulk-rock H_2O content of AC-12 were based on the modal abundance of hydrous minerals (i.e., hornblende and biotite), and are sufficiently high to minimally saturate the solidus at

15251314, 2024, 3, Downloaded from https://onlinelibrary.wiley.com/doi/10.1111/jmg.12759 by Universitat Bern, Wiley Online Library on [13/03/2024]. See the Terms and Conditions (https://onlinelibrary.wiley.com/terms-and-conditions) on Wiley Online Library for rules of use; OA articles are governed by the applicable Creative Commons License

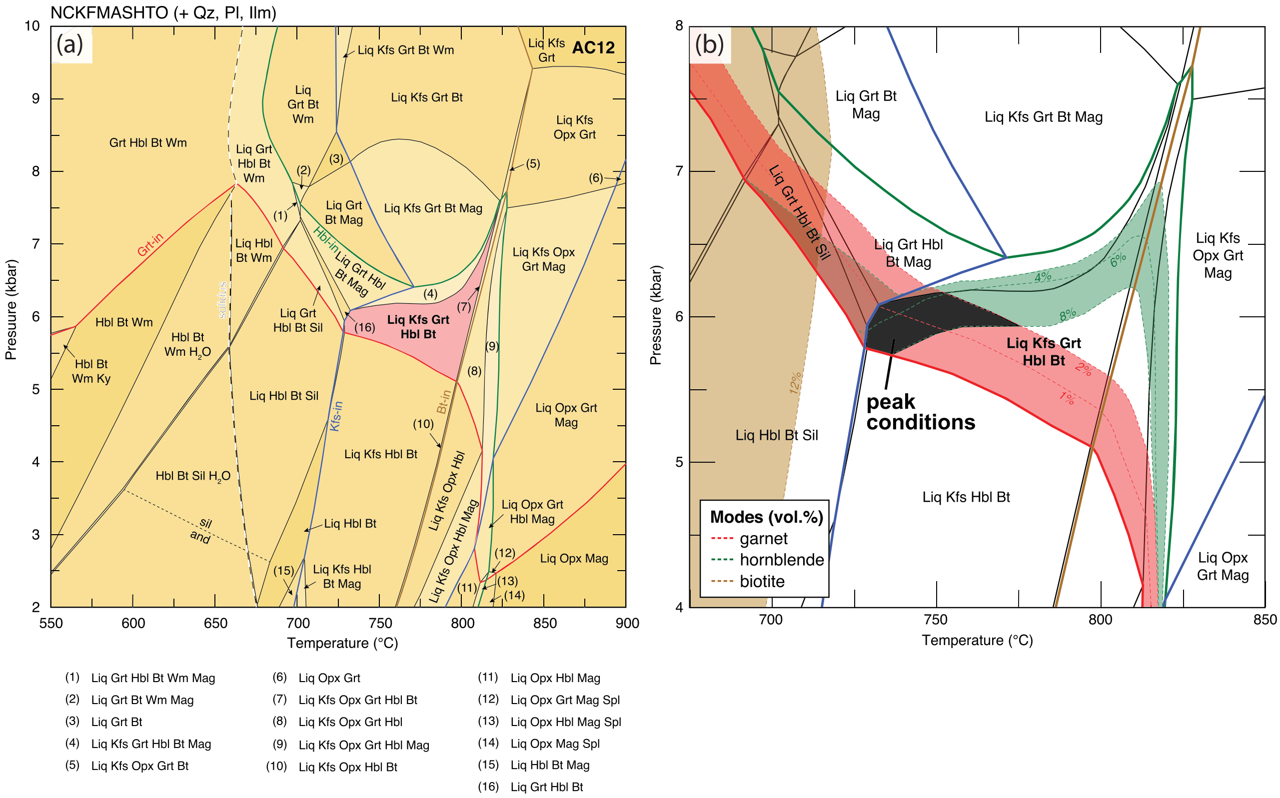

FIGURE 8 (a) *P*–*T* pseudosection for sample AC-12. The observed mineral assemblage is marked by the red field. Stability of key minerals is indicated by coloured curves: red – garnet, blue – K-feldspar, green – hornblende, brown – biotite, white dashed – solidus. (b) Close-up of the peak field contoured for the observed modes of garnet, hornblende and biotite with an arbitrary uncertainty envelope of ±1 vol.% for garnet and ±2 vol.% for hornblende and biotite. Intersection of garnet and hornblende modes constrain the metamorphic peak conditions to 725–775°C and 5.7–6.2 kbar.

5.5 kbar. The observed phase assemblage is predicted to be stable from 760 to 800°C for this composition. Nonetheless, slightly lower bulk-rock H_2O contents for both samples during peak metamorphism would be consistent with the possibility of some prograde subsolidus growth of garnet and retrograde growth of biotite ± hornblende.

Variations in oxidation of the protolith and the implication for phase stabilities are illustrated in Figure 9b. A bulk-rock composition with $X_{Fe^{3+}} = 0.10$, such as assumed for the construction of the *P*–*T* pseudosections in Figure 8, reproduces the observed mineral assemblage of sample AC-12 between ~765 and 800°C. The peak field is constrained to relatively reduced compositions ($X_{Fe^{3+}} < 0.12$) to account for the presence of garnet, which shows an inverse relationship to that observed for K-feldspar. The stability of both hornblende and biotite is largely unaffected by variations in $X_{Fe^{3+}}$ over the modelled range, whereas magnetite only occurs in compositions with $X_{Fe^{3+}} > 0.125$ below ~825°C, consistent with its absence in the observed peak assemblage.

4.1.7 | Lu–Hf geochronology

Sixty-eight and 69 analyses for Lu–Hf geochronology were acquired on garnet fragments from samples AC-13 and AC-12, respectively. The full dataset including standards and unknowns is provided in the supplementary material S2. The number of spots analysed per grain typically varied between one and three, limited by the small size of the fragments (100–500 μm). Garnet from sample AC-13 is characterized by ratios of $^{176}Lu/^{176}Hf$ and $^{177}Hf/^{176}Hf$ ranging from 9.803 to 17.391, and from 0.148 to 1.844, respectively. Inspection of the signal from 12 analyses indicated contamination/mixing with other Hf-bearing phases; these data were omitted from the age calculation and are not considered further. Assuming that analyses with the lowest $^{176}Lu/^{176}Hf$ represent the best estimate for the maximum timing of garnet growth, inverse isochron regression of these data yields an age of 3278 ± 33 Ma ($\text{MSWD} = 2.7$, $n = 41$) with an initial $^{176}Hf/^{177}Hf$ ratio of 0.281 ± 0.004 (Figure 10a). Analyses with significantly higher $^{176}Lu/^{176}Hf$ are considered to be

15251314, 2024, 3, Downloaded from https://onlinelibrary.wiley.com/doi/10.1111/jmg.12759 by Universitat Bern, Wiley Online Library on [13/03/2024]. See the Terms and Conditions (https://onlinelibrary.wiley.com/terms-and-conditions) on Wiley Online Library for rules of use; OA articles are governed by the applicable Creative Commons License

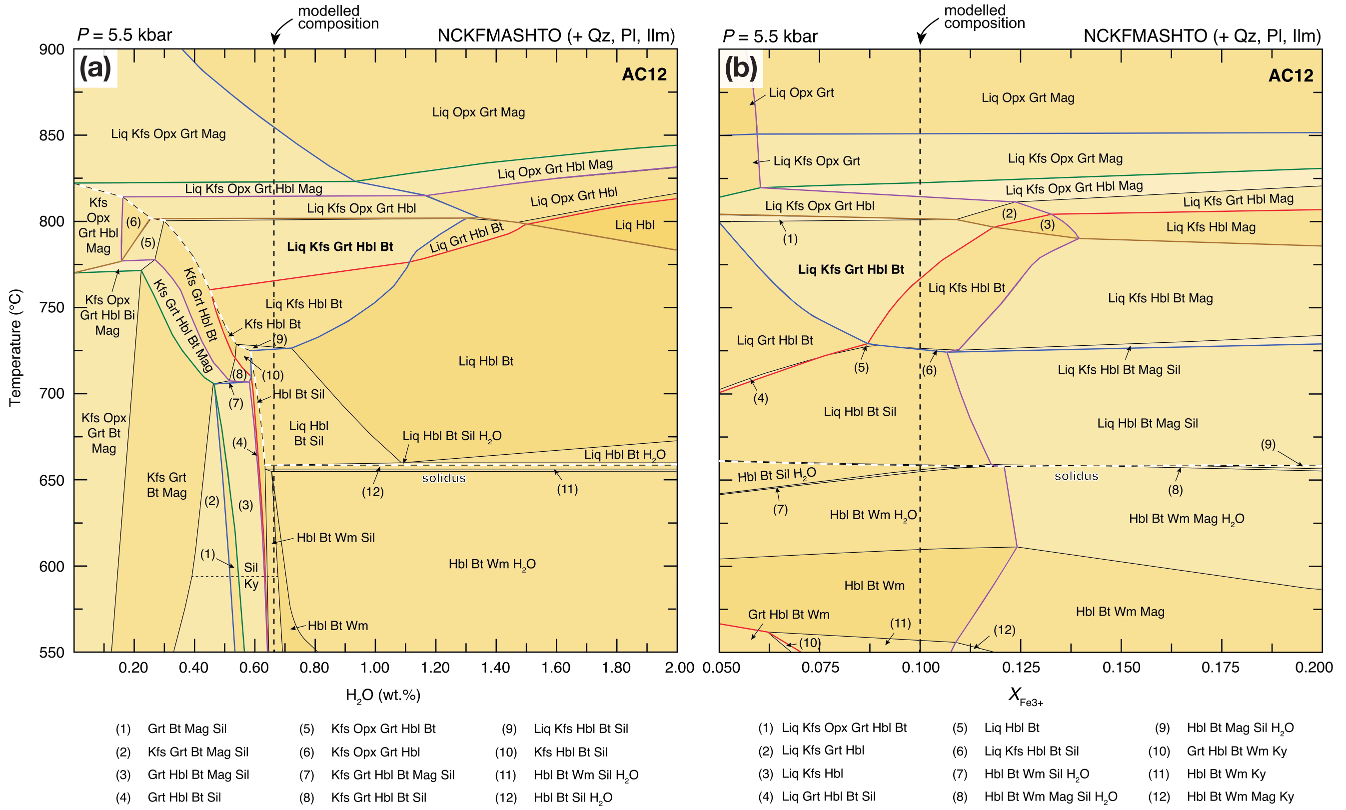

FIGURE 9 (a) T–H_2O and (b) T–$X_{Fe^{3+}}$ pseudosection for sample AC-12 showing the effects of varying bulk-rock water contents and oxidation state on the stability of modelled phase assemblages. Composition used for the construction of the P–T pseudosection is indicated by the vertical dashed line. The observed peak phase assemblage is highlighted in bold. Coloured curves mark the stability of key minerals: red – garnet, blue – K-feldspar, green – hornblende, brown – biotite, magenta – magnetite, white dashed – solidus.

affected by post-crystallization diffusion and were omitted in the isochron regression.

Garnet in sample AC-12 displays a similar spread in $^{177}Hf/^{176}Hf$ but reaches significantly higher $^{176}Lu/^{176}Hf$ ratios than sample AC-13, ranging from 13.817 to 30.039. After rejecting ten analyses affected by mixing with other Hf-bearing phases, this sample yields an inverse errorchron age of 2661 ± 22 Ma ($n = 60$) with an initial $^{176}Hf/^{177}Hf$ ratio of 0.282 ± 0.004 (supplementary material S3). However, an MSWD of 30 for this errorchron implies significant over-dispersion of the data such that this age is likely geologically meaningless. Closer inspection of the data in the inverse isochron space reveals that the Lu–Hf analyses instead appear to scatter between two different trends (Figure 10b, c). Such behaviour may result from either the mixing of different garnet age components and/or open-system behaviour of the Lu–Hf systematics after garnet formation (e.g., Kelly et al., 2011), as discussed below. Dividing the garnet Lu–Hf data into two age populations based on the regression trends of analyses with higher $^{177}Hf/^{176}Hf$ ratios, this sample yields isochron ages of 3214 ± 64 Ma (MSWD = 1.7, $n = 8$) and 1859 ± 38 Ma (MSWD = 1.5, $n = 20$), with a corresponding initial $^{176}Hf/^{177}Hf$ ratio of 0.282 ± 0.004 (Figure 10b–c).

5 | DISCUSSION

5.1 | Pressure–temperature constraints for late Paleoarchean high-grade metamorphism in the AGC

To date, there are no quantitative constraints on the P–T conditions of Archean metamorphism in rocks of the AGC, hampering the reconstruction of their post-magmatic history. Here, we conducted phase equilibrium modelling for two tonalitic gneisses from the oldest crustal component in the AGC (samples AC-13 and AC-12), which we infer to have experienced a common tectono-metamorphic evolution.

Considering minimum uncertainties on P–T of 1 kbar and 50°C and uncertainties in the activity–composition (a–x) models for complex phases such as amphibole

15251314, 2024, 3, Downloaded from https://onlinelibrary.wiley.com/doi/10.1111/jmg.12759 by Universitat Bern, Wiley Online Library on [13/03/2024]. See the Terms and Conditions (https://onlinelibrary.wiley.com/terms-and-conditions) on Wiley Online Library for rules of use; OA articles are governed by the applicable Creative Commons License

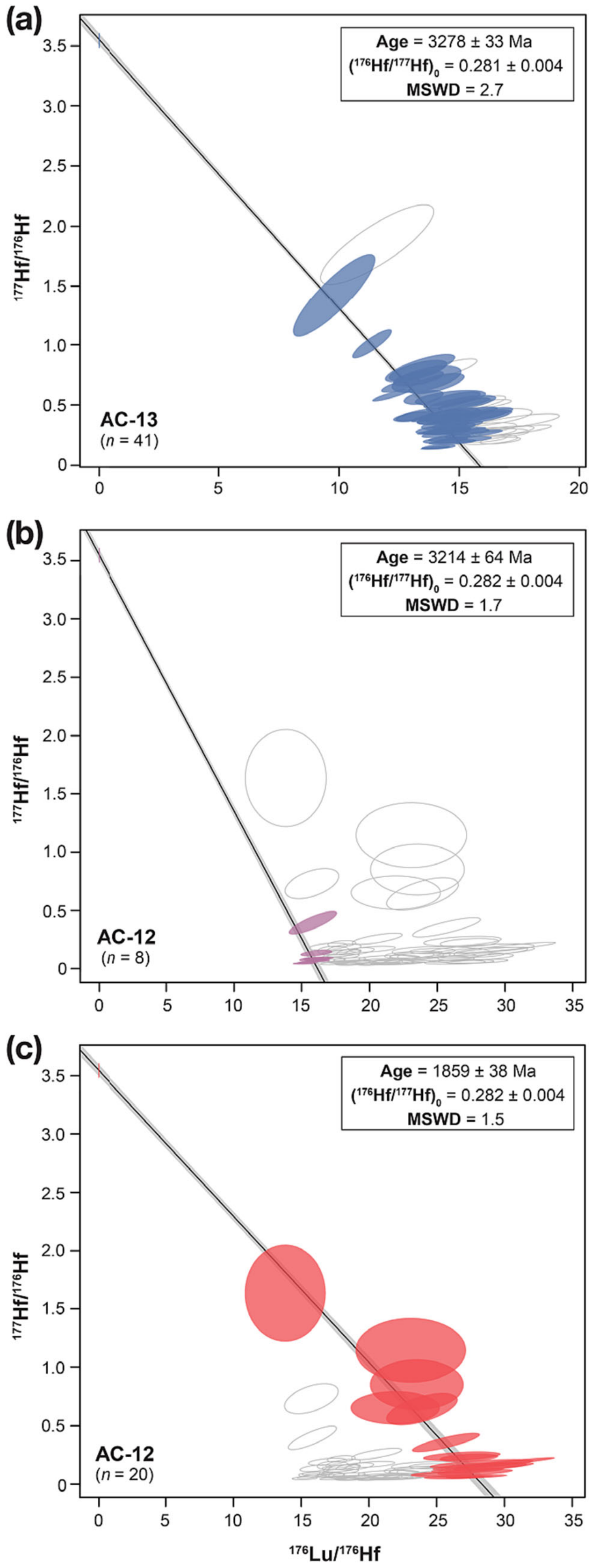

FIGURE 10 Inverse Lu–Hf isochron ages for garnet in sample (a) AC-13 and (b–c) AC-12. Garnet analyses of sample AC-12 are split into two endmembers to differentiate the garnet formation age (Archean) and subsequent resetting during a later (Paleoproterozoic) tectono-metamorphic event. Empty ellipses represent analyses that were not included in the respective isochron regression due to mixing between the two age components but are shown for completeness. Error ellipses are shown at the 2σ level.

(Forshaw et al., 2019), the two rocks give consistent results, recording upper-amphibolite to granulite-facies metamorphism at temperatures of 725–780°C and pressures of 4.5–6.2 kbar (Figure 11). Accepting that sample AC-12 records more retrograde replacement of garnet and hornblende by biotite, the observed and calculated phase proportions are remarkably similar for both samples (Figure 6), suggesting the calculated *P*–*T* conditions are reliable.

The thermobaric ratios (*T*/*P*) of the two samples at their metamorphic peak conditions correspond to high apparent thermal gradients between 125 and 155°C/kbar for the late Paleoarchean metamorphic event (Figure 11). Considering that both samples likely record a common *P*–*T* evolution, and assuming the uncertainties discussed above, we take a mean value of 140°C/kbar to be representative of the apparent thermal gradient during metamorphism of the tonalitic gneisses in the AGC. Although this value is the highest recovered from any Paleoarchean-Mesoarchean crust so far, it is broadly similar to those recorded by several other Archean high-grade gneiss terranes where metamorphic conditions have been constrained (Brown & Johnson, 2019), such as for Mesoarchean metamorphism of the Mahamba Gneiss Complex in Swaziland (Suhr et al., 2015; Taylor et al., 2012) and Paleoarchean metamorphism of the Itsaq Gneiss Complex in southwest Greenland (Horie et al., 2010; Nutman et al., 2020) (Figure 11). These terranes are generally thought to represent segments of mid to lower continental crust that have experienced extensive partial melting (intracrustal reworking), resulting in the generation of significant quantities of tonalitic to granitic melt by hornblende and/or biotite breakdown (Moyen, 2011; Moyen & Martin, 2012; White et al., 2017). Although voluminous granitic bodies that are temporally related to Paleoarchean high-grade metamorphism in the AGC have so far not been reported in the eastern low-strain domain, recent data from the detrital zircon record suggest that significant volumes of the unmapped AGC basement are comprised of 3.37 Ga granitoids (Bilak et al., 2022). We argue that pervasive partial melting at deeper crustal levels at that time could have led to

15251314, 2024, 3, Downloaded from https://onlinelibrary.wiley.com/doi/10.1111/jmg.12759 by Universitat Bern, Wiley Online Library on [13/03/2024]. See the Terms and Conditions (https://onlinelibrary.wiley.com/terms-and-conditions) on Wiley Online Library for rules of use; OA articles are governed by the applicable Creative Commons License

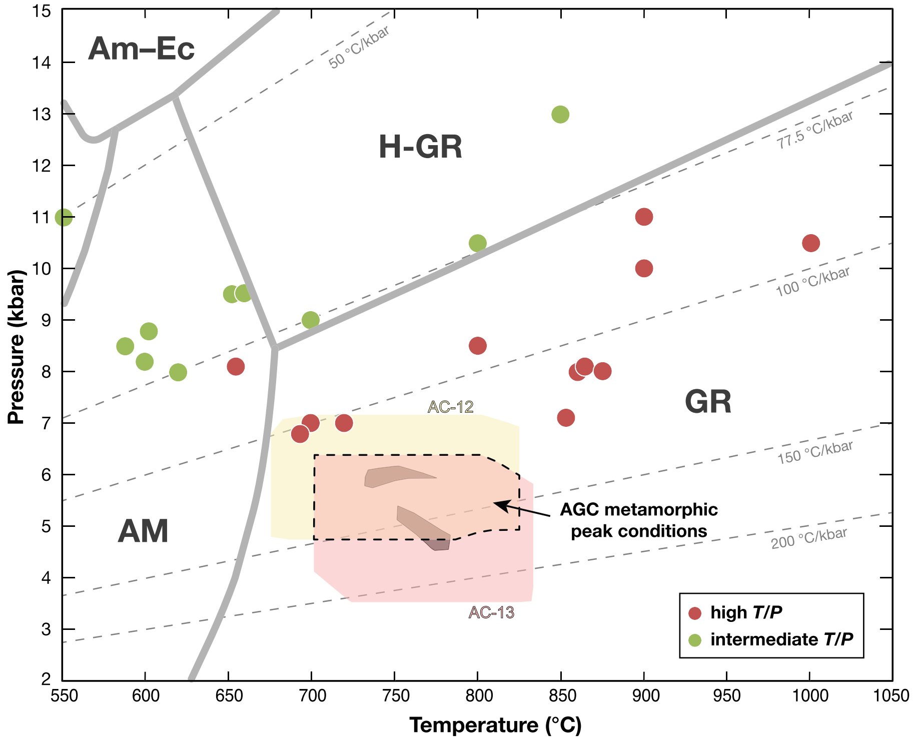

FIGURE 11 Comparison of the inferred metamorphic peak *P–T* conditions for samples investigated in this study and other published estimates for metamorphic rocks older than 2.8 Ga (from Brown & Johnson, 2019; dataset update from October 2023). Individual peak *P–T* conditions for AC-13 and AC-12 were constrained by the intersection of modal isopleths of garnet, hornblende and biotite within the assumed peak field and are indicated by grey polygons. Uncertainties of 1 kbar and 50°C on the position of peak fields are indicated by coloured polygons. Estimates for the peak metamorphic conditions in the AGC are given by the area intersecting both fields (dashed outline). Selected thermobaric gradients are shown by grey dashed lines. AM – amphibolite, Am–Ec – amphibolite–eclogite, H-GR – high-pressure granulite, GR – granulite.

widespread emplacement of such granitic bodies into higher crustal levels, inducing high-grade metamorphism of the surrounding tonalitic gneisses and local partial melting at elevated thermal gradients.

Assuming closed-system behaviour during partial melting of these rocks, melt fractions for sample AC-13 and AC-12 at metamorphic peak conditions are predicted to be only ~6 vol.% and ~4 vol.%, respectively. Melt volumes below the melt connectivity transition (7 vol.%; Rosenberg & Handy, 2005) are typically restricted to grain boundaries and isolated melt pockets, such that any partial melt generated in situ below this threshold during prograde metamorphism may not have been lost, but instead remained to crystallize in the host rocks.

5.2 | Lu–Hf garnet geochronology and implications for isotopic disturbance in the AGC

The Lu–Hf isotope data from garnet in tonalitic gneisses from the AGC exhibit significant scatter and large MSWDs, consistent with disturbance of the Lu–Hf systematics by a later tectono-thermal event(s), and/or age mixing between different generations of garnet. The absence of any clear systematic correlation between the measured isotope ratios and the monitored element abundances (e.g., of Ca, Ti and HREE) suggests that the observed scatter most likely does not record the mixing of different garnet populations of varying age. This is in agreement with petrographic observations that show no evidence for the existence of multiple garnet generations in either sample. Rather, the compositional zoning in maps and along transects (Figure 3c–d) are more compatible with intracrystalline diffusion and partial re-equilibration of primary growth zoning during cooling and resorption of garnet that led to partial resetting of the Lu–Hf systematics and the observed scatter. A single stage of garnet growth over a narrow *P–T* interval close to the predicted metamorphic peak is supported by the calculated phase equilibria (Figure 5, Figure 8).

Isochron regression of the Lu–Hf garnet data from sample AC-13 constrains the age of high-grade metamorphism in the AGC to *c.* 3.28 Ga (Figure 10a). A minor

15251314, 2024, 3, Downloaded from https://onlinelibrary.wiley.com/doi/10.1111/jmg.12759 by Universitat Bern, Wiley Online Library on [13/03/2024]. See the Terms and Conditions (https://onlinelibrary.wiley.com/terms-and-conditions) on Wiley Online Library for rules of use; OA articles are governed by the applicable Creative Commons License

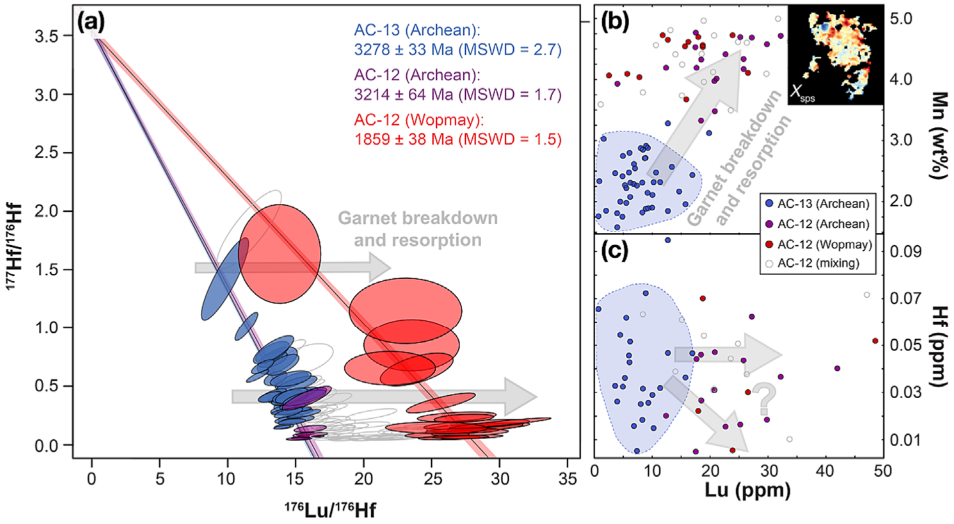

FIGURE 12 Combined inverse Lu–Hf isochron ages for garnet in samples AC-13 and AC-12. Garnet analyses of sample AC-12 are split into two groups to differentiate garnet formation (Archean) and subsequent isotopic disturbance during a later tectono-metamorphic event. Arrows indicate shift of Lu–Hf data due to the retention of Lu and/or loss of Hf during garnet resorption. Empty ellipses represent analyses that are thought to represent mixing between the two age components. (b) Lu concentrations in garnet plotted against Mn as a proxy for progressive garnet re-equilibration, and (c) against Hf. Inset shows X_{sps} map of garnet in AC-12.

shift towards higher ^{176}Lu/^{176}Hf ratios and an MSWD of 2.7 for this sample may record partial modification of the isotope systematics in some of the smaller garnet fragments, such that this age should be considered as a minimum for garnet formation. In sample AC-12, Lu–Hf systematics from those portions of garnet least affected by later re-equilibration yield a similar age of 3,214 ± 64 Ma (Figure 10b), which confirms garnet growth during late Paleoarchean metamorphism. Subsequent disturbance of the Lu–Hf systematics likely occurred during the *c.* 1.9–1.8 Ga Wopmay orogeny, as indicated by isochron regression of the younger age component in sample AC-12 (Figure 10c).

We interpret the observed scatter of Lu–Hf data in sample AC-12 as a record of variable degrees of isotopic disturbance during resorption of garnet as the result of the Paleoproterozoic Wopmay orogeny, consistent with findings of previous studies utilizing whole-rock Lu–Hf (Guitreau et al., 2014) and Sm–Nd data (Fisher et al., 2020; Moorbath et al., 1997), and U–Pb and Sm–Nd data from apatite and titanite (Antoine et al., 2020; Fisher et al., 2020; Sano et al., 1999). U–Pb dating of zircon yields ages between 3.4 and 3.2 Ga for zircon overgrowths and recrystallized domains that are interpreted to date high-grade metamorphism and partial melting in the AGC (Kirkland et al., in review; Reimink et al., 2014; Reimink, Chacko, et al., 2016; Stern & Bleeker, 1998). These ages are in good agreement with the garnet Lu–Hf age obtained in this study, supporting the interpretation that garnet in sample AC-13 was mostly unaffected by later overprinting and reliably dates Paleoarchean metamorphism in the AGC. Moreover, radiogenic lead mobility in zircon has been inferred to reflect metamorphism during the Wopmay orogeny (Kirkland et al., 2020; Sano et al., 1999) and is consistent with the timing of partial resetting of Lu–Hf systematics in garnet from sample AC-12.

We argue that the degree to which the two samples were affected by the Wopmay orogeny is also recorded in the major and trace element composition of garnet (Figure 3, Figure 12). The garnets from sample AC-13, which yield a late Paleoarchean age, are generally well-preserved and display flat compositional profiles characterized by relatively high almandine and low grossular contents. Although the initial zoning of garnet was likely obscured by intracrystalline diffusive relaxation of major elements at elevated temperatures (e.g., Ague & Axler, 2016; Baxter et al., 2017), the slower-diffusing trace elements preserve elevated HREE abundances in the core, which we think largely documents the primary growth history (Figure 3c–d). By contrast, garnets from sample AC-12 are highly resorbed and fragmented and display patchy major element zoning marked by relatively higher grossular and lower almandine contents, which we attribute to retrograde resetting during the *c.* 1.9 Ga Wopmay orogeny. Notably, no clear correlation between the distinct zoning pattern observed in X_{alm} and X_{grs}, and the trace element pattern can be drawn. Instead, the abundances of both Mn and Y + HREE sharply increase along fractures and resorbed grain margins,

15251314, 2024, 3, Downloaded from https://onlinelibrary.wiley.com/doi/10.1111/jmg.12759 by Universitat Bern, Wiley Online Library on [13/03/2024]. See the Terms and Conditions (https://onlinelibrary.wiley.com/terms-and-conditions) on Wiley Online Library for rules of use; OA articles are governed by the applicable Creative Commons License

likely as a result of retrogressive uptake of these elements during garnet resorption (Baxter et al., 2017; Kohn, 2009; Smit et al., 2013). The extent of resorption and isotopic disturbance of the early Paleoarchean garnets may correspond to the local availability of a free fluid phase during retrogression, leading to partial replacement of garnet by plagioclase ± epidote and biotite, and/or to the smaller grain size of garnet in sample AC-12.

Such preferential retention of elements that are compatible in garnet (i.e., HREE) and loss of incompatible elements (i.e., Hf) to the matrix during resorption and re-equilibration clearly has implications for Lu–Hf garnet geochronometry (Kelly et al., 2011). Progressive partitioning of Lu from resorbed rims into the relict garnet will shift initial ^{176}Lu/^{177}Hf ratios towards higher values, whereas the ^{176}Hf/^{177}Hf ratio is expected to retain its composition despite the loss of Hf, producing younger apparent ages. Accordingly, Lu–Hf data will also shift towards higher ^{176}Lu/^{176}Hf ratios (retaining their ^{177}Hf/^{176}Hf ratios) in the inverse isochron diagram, as shown in Figure 12a. Plotting the Lu and Hf concentrations for each Lu–Hf age analysis, alongside their Mn content as a proxy for progressive garnet resorption, should produce a clear distribution between the different age components (Figure 12b–c). Although Mn seems to be a reliable tracer for garnet resorption and re-equilibration of the two samples, the data for AC-12 do not allow us to differentiate between the two age components. In contrast to the trace element profiles, there is no clear correlation between high Lu and Mn concentrations in this sample. Similarly, it is unclear whether the shift towards higher ^{176}Lu/^{176}Hf ratios for the 1.9–1.8 Ga age component was induced by an increase in Lu or by a decrease in Hf, as only 5 of 17 Hf analyses (29%) lie above the detection limit for the youngest age component (Figure 12c). Notwithstanding, due to different spot sizes, the trace element analyses and the Lu–Hf isotope analyses were not obtained from the same volume of garnet, and may therefore not record the same compositional domain. Considering the small-scale patchy zoning observed in AC-12, we argue that obtaining both trace element and age information from the same garnet domain is mostly limited by the large spot size and lower spatial resolution of Lu–Hf analyses.

Finally, we find no evidence for Eoarchean metamorphism in the AGC as previously suggested based on the occurrence of recrystallized zircon domains with ages of 3.75 and 3.6 Ga (Bowring & Williams, 1999; Iizuka et al., 2007). We infer that evidence for these events may have been erased during pervasive high-grade metamorphism at 3.3–3.2 Ga, even though some Hadean to Eoarchean zircons apparently escaped recrystallization and lead loss.

Paleoarchean metamorphism in the AGC records thermobaric ratios that are warmer than, but broadly similar to other samples of Paleoarchean-Mesoarchean age (Brown & Johnson, 2019). The absence of evidence for bimodal metamorphism and/or rocks characteristic of low *T/P* metamorphism (such as eclogite and blueschist) in the crustal record older than 2.8 Ga should not be used by itself as evidence for the absence of plate tectonics on the early Earth. However, the unimodal distribution of *T/P* in the Archean metamorphic record may be more consistent with non-plate-tectonic (sluggish or stagnant lid) modes (Holder et al., 2019).

6 | CONCLUSIONS

1. Phase equilibrium modelling of two garnet-bearing tonalitic gneisses indicates that the Acasta Gneiss Complex experienced upper-amphibolite to granulite-facies metamorphism with peak conditions of $T = 725$–780°C and $P = 4.5$–6.2 kbar.
2. Laser-ablation Lu–Hf geochronology of garnet constrains the age of this tectono-metamorphic event to *c.* 3.3–3.2 Ga and supports earlier studies that argued for high-grade metamorphism inducing partial melting and isotopic disturbance in the AGC at that time.
3. Metamorphic peak conditions suggest a high apparent thermal gradient of ~140°C/kbar for late Paleoarchean metamorphism, which is consistent with the *T/P* gradients for other examples of Paleoarchean-Mesoarchean crustal metamorphism.
4. Garnet shows evidence for partial re-equilibration and concomitant disturbance of the Lu–Hf systematics in response to the *c.* 1.9–1.8 Ga Wopmay orogeny.

ACKNOWLEDGMENTS

We thank L. Morrissey and J. Mulder for their reviews, and J. Diener for his proficient editorial handling. Financial support from Curtin University and Australian Research Council grant DP200101104 to TEJ and CC is gratefully acknowledged. Open access publishing facilitated by Curtin University, as part of the Wiley - Curtin University agreement via the Council of Australian University Librarians.

CONFLICT OF INTEREST STATEMENT

The authors declare no conflicts of interest relevant to this study.

DATA AVAILABILITY STATEMENT

The data that support the findings of this study are available in the supplementary materials of this article (S1–S3).

15251314, 2024, 3, Downloaded from https://onlinelibrary.wiley.com/doi/10.1111/jmg.12759 by Universitat Bern, Wiley Online Library on [13/03/2024]. See the Terms and Conditions (https://onlinelibrary.wiley.com/terms-and-conditions) on Wiley Online Library for rules of use; OA articles are governed by the applicable Creative Commons License

ORCID

Jonas Kaempf https://orcid.org/0000-0003-1837-1048
Tim E. Johnson https://orcid.org/0000-0001-8704-4396
Chris Clark https://orcid.org/0000-0001-9982-7849

REFERENCES

Aarons, S. M., Reimink, J. R., Greber, N. D., Heard, A. W., Zhang, Z., & Dauphas, N. (2020). Titanium isotopes constrain a magmatic transition at the Hadean-Archean boundary in the Acasta gneiss complex. *Science Advances*, *6*, eabc9959. https://doi.org/10.1126/sciadv.abc9959

Ague, J. J., & Axler, J. A. (2016). Interface coupled dissolution-reprecipitation in garnet from subducted granulites and ultrahigh-pressure rocks revealed by phosphorous, sodium, and titanium zonation. *American Mineralogist*, *101*, 1696–1699. https://doi.org/10.2138/am-2016-5707

Antoine, C., Bruand, E., Guitreau, M., & Devidal, J.-L. (2020). Understanding preservation of primary signatures in apatite by comparing matrix and zircon-hosted crystals from the Eoarchean Acasta gneiss complex (Canada). *Geochemistry, Geophysics, Geosystems*, *21*, e2020GC008923. https://doi.org/10.1029/2020GC008923

Bauer, A. M., Fisher, C. M., Vervoort, J. D., & Bowring, S. A. (2017). Coupled zircon Lu–Hf and U–Pb isotopic analyses of the oldest terrestrial crust, the >4.03 Ga Acasta gneiss complex. *Earth and Planetary Science Letters*, *458*, 37–48. https://doi.org/10.1016/j.epsl.2016.10.036

Bauer, A. M., Vervoort, J. D., & Fisher, C. M. (2020). Unraveling the complexity of zircons from the 4.0–2.9 Ga Acasta gneiss complex. *Geochimica et Cosmochimica Acta*, *283*, 85–102. https://doi.org/10.1016/j.gca.2020.05.023

Baxter, E. F., Caddick, M. J., & Dragovic, B. (2017). Garnet: A rock-forming mineral petrochronometer. *Reviews in Mineralogy and Geochemistry*, *83*, 469–533. https://doi.org/10.2138/rmg.2017.83.15

Bédard, J. H. (2018). Stagnant lids and mantle overturns: Implications for Archaean tectonics, magmagenesis, crustal growth, mantle evolution, and the start of plate tectonics. *Geoscience Frontiers*, *9*, 19–49. https://doi.org/10.1016/j.gsf.2017.01.005

Bilak, G. S., Niemetz, K., Reimink, J. R., Reyes, A. V., Chacko, T., DuFrane, S. A., Belosevic, M., & Ketchum, J. W. F. (2022). Evaluating the age distribution of exposed crust in the Acasta gneiss complex using detrital zircons in Pleistocene eskers. *Geochemistry, Geophysics, Geosystems*, *23*, e2022GC010380. https://doi.org/10.1029/2022GC010380

Bowring, S. A., & Housh, T. (1995). The Earth's early evolution. *Science*, *269*, 1535–1540. https://doi.org/10.1126/science.7667634

Bowring, S. A., King, J. E., Housh, T. B., Isachsen, C. E., & Podosek, F. A. (1989). Neodymium and lead isotope evidence for enriched early Archaean crust in North America. *Nature*, *340*, 222–225. https://doi.org/10.1038/340222a0

Bowring, S. A., & Williams, I. S. (1999). Priscoan (4.00-4.03 Ga) orthogneisses from northwestern Canada. *Contributions to Mineralogy and Petrology*, *134*, 3–16. https://doi.org/10.1007/s004100050465

Bowring, S. A., Williams, I. S., & Compston, W. (1989). 3.96 Ga gneisses from the slave province, Northwest Territories, Canada. *Geology*, *17*, 971. https://doi.org/10.1130/0091-7613(1989)017<0971:GGFTSP>2.3.CO;2

Boynton, W. V. (1984). Chapter 3 - Cosmochemistry of the rare earth elements: Meteorite studies. In P. Henderson (Ed.), *Developments in geochemistry* (pp. 63–114). Elsevier.

Brown, D. A., Simpson, A., Hand, M., Morrissey, L. J., Gilbert, S., Tamblyn, R., & Glorie, S. (2022). Laser-ablation Lu-Hf dating reveals Laurentian garnet in subducted rocks from southern Australia. *Geology*, *50*, 837–842. https://doi.org/10.1130/G49784.1

Brown, M., & Johnson, T. (2018). Secular change in metamorphism and the onset of global plate tectonics. *American Mineralogist*, *103*, 181–196. https://doi.org/10.2138/am-2018-6166

Brown, M., & Johnson, T. (2019). Time's arrow, time's cycle: Granulite metamorphism and geodynamics. *Mineralogical Magazine*, *83*, 323–338. https://doi.org/10.1180/mgm.2019.19

Brown, M., Johnson, T., & Gardiner, N. J. (2020). Plate tectonics and the Archean earth. *Annual Review of Earth and Planetary Sciences*, *48*, 291–320. https://doi.org/10.1146/annurev-earth-081619-052705

Connolly, J. (1990). Multivariable phase diagrams: An algorithm based on generalized thermodynamics. *American Journal of Science*, *290*, 666–718. https://doi.org/10.2475/ajs.290.6.666

Connolly, J. A. D. (2005). Computation of phase equilibria by linear programming: A tool for geodynamic modeling and its application to subduction zone decarbonation. *Earth and Planetary Science Letters*, *236*, 524–541. https://doi.org/10.1016/j.epsl.2005.04.033

Connolly, J. A. D. (2009). The geodynamic equation of state: What and how. *Geochemistry, Geophysics, Geosystems*, *10*, 10. https://doi.org/10.1029/2009GC002540

Davidek, K. L., Martin, M. W., Bowring, S. A., & Williams, I. S. (1997). *Conventional U-Pb geochronology of the Acasta gneisses using single crystal zircon fragmentation technique (abstract)*. Geological Association of Canada.

De Biévre, P., & Taylor, P. D. P. (1993). Table of the isotopic compositions of the elements. *International Journal of Mass Spectrometry and Ion Processes*, *123*, 149–166. https://doi.org/10.1016/0168-1176(93)87009-H

Diener, J. F. A., & Powell, R. (2010). Influence of ferric iron on the stability of mineral assemblages. *Journal of Metamorphic Geology*, *28*, 599–613. https://doi.org/10.1111/j.1525-1314.2010.00880.x

Fisher, C. M., Bauer, A. M., & Vervoort, J. D. (2020). Disturbances in the Sm–Nd isotope system of the Acasta gneiss complex—Implications for the Nd isotope record of the early earth. *Earth and Planetary Science Letters*, *530*, 115900. https://doi.org/10.1016/j.epsl.2019.115900

Forshaw, J., Waters, D., Pattison, D., Palin, R., & Gopon, P. (2019). A comparison of observed and thermodynamically predicted phase equilibria and mineral compositions in mafic granulites. *Journal of Metamorphic Geology*, *37*, 153–179. https://doi.org/10.1111/jmg.12454

Green, E. C. R., White, R. W., Diener, J. F. A., Powell, R., Holland, T. J. B., & Palin, R. M. (2016). Activity-composition relations for the calculation of partial melting equilibria in metabasic rocks. *Journal of Metamorphic Geology*, *34*, 845–869. https://doi.org/10.1111/jmg.12211

Guiraud, M., Powell, R., & Rebay, G. (2001). H_2O in metamorphism and unexpected behaviour in the preservation of metamorphic mineral assemblages. *Journal of Metamorphic Geology*, *19*, 445–454. https://doi.org/10.1046/j.0263-4929.2001.00320.x

15251314, 2024, 3, Downloaded from https://onlinelibrary.wiley.com/doi/10.1111/jmg.12759 by Universitat Bern, Wiley Online Library on [13/03/2024]. See the Terms and Conditions (https://onlinelibrary.wiley.com/terms-and-conditions) on Wiley Online Library for rules of use; OA articles are governed by the applicable Creative Commons License

Guitreau, M., Blichert-Toft, J., Mojzsis, S. J., Roth, A. S. G., Bourdon, B., Cates, N. L., & Bleeker, W. (2014). Lu–Hf isotope systematics of the Hadean–Eoarchean Acasta gneiss complex (Northwest Territories, Canada). *Geochimica et Cosmochimica Acta*, *135*, 251–269. https://doi.org/10.1016/j.gca.2014.03.039

Hastie, A. R., Fitton, J. G., Bromiley, G. D., Butler, I. B., & Odling, N. W. A. (2016). The origin of Earth's first continents and the onset of plate tectonics. *Geology*, *44*, 855–858. https://doi.org/10.1130/G38226.1

Hawthorne, F., Oberti, R., Harlow, G., Maresch, W., Martin, R., Schumacher, J., & Welch, M. (2012). Nomenclature of the amphibole supergroup. *American Mineralogist*, *97*, 2031–2048. https://doi.org/10.2138/am.2012.4276

Hodges, K. V., Bowring, S. A., Coleman, D. S., Hawkins, D. P., & Davidek, K. L. (1995). Multi-stage thermal history of the ca. 4.0 Ga Acasta gneisses. paper presented at the American Geophysical Union, Fall Meeting. San Francisco, California.

Hoffman, P. F., & Bowring, S. A. (1984). Short-lived 1.9 Ga continental margin and its destruction, Wopmay orogen, Northwest Canada. *Geology*, *12*, 68–72. https://doi.org/10.1130/0091-7613(1984)12<68:SGCMAI>2.0.CO;2

Holder, R. M., Viete, D. R., Brown, M., & Johnson, T. E. (2019). Metamorphism and the evolution of plate tectonics. *Nature*, *572*, 378–381. https://doi.org/10.1038/s41586-019-1462-2

Holland, T., & Powell, R. (2003). Activity-composition relations for phases in petrological calculations: An asymmetric multicomponent formulation. *Contributions to Mineralogy and Petrology*, *145*, 492–501. https://doi.org/10.1007/s00410-003-0464-z

Holland, T. J. B., & Powell, R. (2011). An improved and extended internally consistent thermodynamic dataset for phases of petrological interest, involving a new equation of state for solids. *Journal of Metamorphic Geology*, *29*, 333–383. https://doi.org/10.1111/j.1525-1314.2010.00923.x

Horie, K., Nutman, A. P., Friend, C. R. L., & Hidaka, H. (2010). The complex age of orthogneiss protoliths exemplified by the Eoarchaean Itsaq gneiss complex (Greenland): SHRIMP and old rocks. *Precambrian Research*, *183*, 25–43. https://doi.org/10.1016/j.precamres.2010.06.016

Howell, D., Griffin, W. L., Pearson, N. J., Powell, W., Wieland, P., & O'Reilly, S. Y. (2013). Trace element partitioning in mixed-habit diamonds. *Chemical Geology*, *355*, 134–143. https://doi.org/10.1016/j.chemgeo.2013.07.013

Iizuka, T., Horie, K., Komiya, T., Maruyama, S., Hirata, T., Hidaka, H., & Windley, B. F. (2006). 4.2 Ga zircon xenocryst in an Acasta gneiss from northwestern Canada: Evidence for early continental crust. *Geology*, *34*, 245–248. https://doi.org/10.1130/G22124.1

Iizuka, T., Komiya, T., Johnson, S. P., Kon, Y., Maruyama, S., & Hirata, T. (2009). Reworking of Hadean crust in the Acasta gneisses, northwestern Canada: Evidence from in-situ Lu–Hf isotope analysis of zircon. *Chemical Geology*, *259*, 230–239. https://doi.org/10.1016/j.chemgeo.2008.11.007

Iizuka, T., Komiya, T., Ueno, Y., Katayama, I., Uehara, Y., Maruyama, S., Hirata, T., Johnson, S. P., & Dunkley, D. J. (2007). Geology and zircon geochronology of the Acasta gneiss complex, northwestern Canada: New constraints on its tectonothermal history. *Precambrian Research*, *153*, 179–208. https://doi.org/10.1016/j.precamres.2006.11.017

Jochum, K. P., Nohl, U., Herwig, K., Lammel, E., Stoll, B., & Hofmann, A. W. (2005). GeoReM: A new geochemical database for reference materials and isotopic standards. *Geostandards and Geoanalytical Research*, *29*, 333–338. https://doi.org/10.1111/j.1751-908X.2005.tb00904.x

Johnson, T. E., Brown, M., Gardiner, N. J., Kirkland, C. L., & Smithies, R. H. (2017). Earth's first stable continents did not form by subduction. *Nature*, *543*, 239–242. https://doi.org/10.1038/nature21383

Johnson, T. E., Brown, M., Kaus, B. J. P., & VanTongeren, J. A. (2014). Delamination and recycling of Archaean crust caused by gravitational instabilities. *Nature Geoscience*, *7*, 47–52. https://doi.org/10.1038/ngeo2019

Kelly, E. D., Carlson, W. D., & Connelly, J. N. (2011). Implications of garnet resorption for the Lu–Hf garnet geochronometer: An example from the contact aureole of the Makhavinekh Lake pluton, Labrador. *Journal of Metamorphic Geology*, *29*, 901–916. https://doi.org/10.1111/j.1525-1314.2011.00946.x

Kirkland, C. L., Johnson, T. E., Gillespie, J., Martin, L., Rankenburg, K., Kaempf, J., & Clark, C. (in review). Growth of crustal nuclei through top-down melting on the early earth. *Nature Communications*, *625*, 2024.

Kirkland, C. L., Johnson, T. E., Kinny, P. D., & Kapitany, T. (2020). Modelling U-Pb discordance in the Acasta gneiss: Implications for fluid–rock interaction in Earth's oldest dated crust. *Gondwana Research*, *77*, 223–237. https://doi.org/10.1016/j.gr.2019.07.017

Kohn, M. J. (2009). Models of garnet differential geochronology. *Geochimica et Cosmochimica Acta*, *73*, 170–182. https://doi.org/10.1016/j.gca.2008.10.004

Korenaga, J. (2021). Hadean geodynamics and the nature of early continental crust. *Precambrian Research*, *359*, 106178. https://doi.org/10.1016/j.precamres.2021.106178

Lanari, P., & Duesterhoeft, E. (2019). Modeling metamorphic rocks using equilibrium thermodynamics and internally consistent databases: Past achievements, problems and perspectives. *Journal of Petrology*, *60*, 19–56. https://doi.org/10.1093/petrology/egy105

Lanari, P., & Engi, M. (2017). Local bulk composition effects on metamorphic mineral assemblages. *Reviews in Mineralogy and Geochemistry*, *83*, 55–102. https://doi.org/10.2138/rmg.2017.83.3

Lanari, P., & Piccoli, F. (2020). New horizons in quantitative compositional mapping – Analytical conditions and data reduction using XMapTools. *IOP Conference Series: Materials Science and Engineering*, *891*, 012016. https://doi.org/10.1088/1757-899X/891/1/012016

Lanari, P., Vho, A., Bovay, T., Airaghi, L., & Centrella, S. (2019). Quantitative compositional mapping of mineral phases by electron probe micro-analyser. *Geological Society, London, Special Publications*, *478*, 39–63. https://doi.org/10.1144/SP478.4

Lanari, P., Vidal, O., De Andrade, V., Dubacq, B., Lewin, E., Grosch, E. G., & Schwartz, S. (2014). XMapTools: A MATLAB©-based program for electron microprobe X-ray image processing and geothermobarometry. *Computers & Geosciences*, *62*, 227–240. https://doi.org/10.1016/j.cageo.2013.08.010

Li, Y., & Vermeesch, P. (2021). Short communication: Inverse isochron regression for Re–Os, K–Ca and other chronometers. *Geochronology*, *3*, 415–420. https://doi.org/10.5194/gchron-3-415-2021

Miocevich, S. R., Copley, A., & Weller, O. M. (2022). Testing the importance of sagduction: Insights from the Lewisian gneiss

15251314, 2024, 3, Downloaded from https://onlinelibrary.wiley.com/doi/10.1111/jmg.12759 by Universitat Bern, Wiley Online Library on [13/03/2024]. See the Terms and Conditions (https://onlinelibrary.wiley.com/terms-and-conditions) on Wiley Online Library for rules of use; OA articles are governed by the applicable Creative Commons License

complex of Northwest Scotland. *Precambrian Research*, *379*, 106708. https://doi.org/10.1016/j.precamres.2022.106708

Mojzsis, S. J., Cates, N. L., Caro, G., Trail, D., Abramov, O., Guitreau, M., Blichert-Toft, J., Hopkins, M. D., & Bleeker, W. (2014). Component geochronology in the polyphase ca. 3920Ma Acasta gneiss. *Geochimica et Cosmochimica Acta*, *133*, 68–96. https://doi.org/10.1016/j.gca.2014.02.019

Moorbath, S., Whitehouse, M. J., & Kamber, B. S. (1997). Extreme Nd-isotope heterogeneity in the early Archaean — Fact or fiction? Case histories from northern Canada and West Greenland. *Chemical Geology*, *135*, 213–231. https://doi.org/10.1016/S0009-2541(96)00117-9

Moyen, J.-F. (2011). The composite Archaean grey gneisses: Petrological significance, and evidence for a non-unique tectonic setting for Archaean crustal growth. *Lithos*, *123*, 21–36. https://doi.org/10.1016/j.lithos.2010.09.015

Moyen, J.-F., & Martin, H. (2012). Forty years of TTG research. *Lithos*, *148*, 312–336. https://doi.org/10.1016/j.lithos.2012.06.010

Nebel, O., Morel, M. L. A., & Vroon, P. Z. (2009). Isotope dilution determinations of Lu, Hf, Zr, Ta and W, and Hf isotope compositions of NIST SRM 610 and 612 glass wafers. *Geostandards and Geoanalytical Research*, *33*, 487–499. https://doi.org/10.1111/j.1751-908X.2009.00032.x

Nutman, A. P., Bennett, V. C., Friend, C. R. L., & Yi, K. (2020). Eoarchean contrasting ultra-high-pressure to low-pressure metamorphisms (<250 to >1000 °C/GPa) explained by tectonic plate convergence in deep time. *Precambrian Research*, *344*, 105770. https://doi.org/10.1016/j.precamres.2020.105770

Palin, R. M., White, R. W., & Green, E. C. R. (2016). Partial melting of metabasic rocks and the generation of tonalitic–trondhjemitic–granodioritic (TTG) crust in the Archaean: Constraints from phase equilibrium modelling. *Precambrian Research*, *287*, 73–90. https://doi.org/10.1016/j.precamres.2016.11.001

Palin, R. M., White, R. W., Green, E. C. R., Diener, J. F. A., Powell, R., & Holland, T. J. B. (2016). High-grade metamorphism and partial melting of basic and intermediate rocks. *Journal of Metamorphic Geology*, *34*, 871–892. https://doi.org/10.1111/jmg.12212

Paton, C., Hellstrom, J., Paul, B., Woodhead, J., & Hergt, J. (2011). Iolite: Freeware for the visualisation and processing of mass spectrometric data. *Journal of Analytical Atomic Spectrometry*, *26*, 2508–2518. https://doi.org/10.1039/c1ja10172b

Powell, R., & Holland, T. J. B. (2008). On thermobarometry. *Journal of Metamorphic Geology*, *26*, 155–179. https://doi.org/10.1111/j.1525-1314.2007.00756.x

Rayner, N., Stern, R. A., & Carr, S. D. (2005). Grain-scale variations in trace element composition of fluid-altered zircon, Acasta gneiss complex, northwestern Canada. *Contributions to Mineralogy and Petrology*, *148*, 721–734. https://doi.org/10.1007/s00410-004-0633-8

Reimink, J. R., Chacko, T., Stern, R. A., & Heaman, L. M. (2014). Earth's earliest evolved crust generated in an Iceland-like setting. *Nature Geoscience*, *7*, 529–533. https://doi.org/10.1038/ngeo2170

Reimink, J. R., Chacko, T., Stern, R. A., & Heaman, L. M. (2016). The birth of a cratonic nucleus: Lithogeochemical evolution of the 4.02–2.94Ga Acasta gneiss complex. *Precambrian Research*, *281*, 453–472. https://doi.org/10.1016/j.precamres.2016.06.007

Reimink, J. R., Davies, J. H. F. L., Chacko, T., Stern, R. A., Heaman, L. M., Sarkar, C., Schaltegger, U., Creaser, R. A., & Pearson, D. G. (2016). No evidence for Hadean continental crust within Earth's oldest evolved rock unit. *Nature Geoscience*, *9*, 777–780. https://doi.org/10.1038/ngeo2786

Romer, R. L., & Smeds, S.-A. (1996). U-Pb columbite ages of pegmatites from Sveconorwegian terranes in southwestern Sweden. *Precambrian Research*, *76*, 15–30. https://doi.org/10.1016/0301-9268(95)00023-2

Rosenberg, C. L., & Handy, M. R. (2005). Experimental deformation of partially melted granite revisited: Implications for the continental crust. *Journal of Metamorphic Geology*, *23*, 19–28. https://doi.org/10.1111/j.1525-1314.2005.00555.x

Sano, Y., Terada, K., Hidaka, H., Yokoyama, K., & Nutman, A. P. (1999). Palaeoproterozoic thermal events recorded in the ~4.0 Ga Acasta gneiss, Canada: Evidence from SHRIMP U-Pb dating of apatite and zircon. *Geochimica et Cosmochimica Acta*, *63*, 899–905. https://doi.org/10.1016/S0016-7037(98)00303-2

Simpson, A., Gilbert, S., Tamblyn, R., Hand, M., Spandler, C., Gillespie, J., Nixon, A., & Glorie, S. (2021). In-situ LuHf geochronology of garnet, apatite and xenotime by LA ICP MS/MS. *Chemical Geology*, *577*, 120299. https://doi.org/10.1016/j.chemgeo.2021.120299

Simpson, A., Glorie, S., Hand, M., Spandler, C., & Gilbert, S. (2023). Garnet Lu-Hf speed dating: A novel method to rapidly resolve polymetamorphic histories. *Gondwana Research*, *121*, 215–234. https://doi.org/10.1016/j.gr.2023.04.011

Smit, M. A., Scherer, E. E., & Mezger, K. (2013). Lu–Hf and Sm–Nd garnet geochronology: Chronometric closure and implications for dating petrological processes. *Earth and Planetary Science Letters*, *381*, 222–233. https://doi.org/10.1016/j.epsl.2013.08.046

Spear, F. S. (1995). *Metamorphic phase equilibria and pressure-temperature-time paths*. Mineralogical Society of America.

Stern, R., & Bleeker, W. (1998). Age of the world's oldest rocks refined using Canada's SHRIMP: The Acasta gneiss complex, Northwest Territories, Canada. *Geoscience Canada*, *25*, 27–31.

St-Onge, M. R., & Davis, W. J. (2018). Wopmay orogen revisited: Phase equilibria modeling, detrital zircon geochronology, and U-Pb monazite dating of a regional Buchan-type metamorphic sequence. *GSA Bulletin*, *130*, 678–704. https://doi.org/10.1130/B31809.1

Suhr, N., Hoffmann, J. E., Kröner, A., & Schröder, S. (2015). Archaean granulite-facies paragneisses from Central Swaziland: Inferences on Palaeoarchaean crustal reworking and a complex metamorphic history. *Journal of the Geological Society*, *172*, 139–152. https://doi.org/10.1144/jgs2014-007

Taylor, J., Stevens, G., Buick, I. S., & Lana, C. (2012). Successive midcrustal, high-grade metamorphic events provide insight into mid-Archean mountain-building along the SE margin of the proto–Kaapvaal craton. *GSA Bulletin*, *124*, 1191–1211. https://doi.org/10.1130/B30543.1

Vermeesch, P. (2018). IsoplotR: A free and open toolbox for geochronology. *Geoscience Frontiers*, *9*, 1479–1493. https://doi.org/10.1016/j.gsf.2018.04.001

Warr, L. N. (2021). IMA–CNMNC approved mineral symbols. *Mineralogical Magazine*, *85*, 291–320. https://doi.org/10.1180/mgm.2021.43

White, Powell, Holland, & Worley. (2000). The effect of TiO2 and Fe2O3 on metapelitic assemblages at greenschist and amphibolite facies conditions: Mineral equilibria calculations in the system $K_2O–FeO–MgO–Al_2O_3–SiO_2–H_2O–TiO_2–Fe_2O_3$. *Journal of*

15251314, 2024, 3, Downloaded from https://onlinelibrary.wiley.com/doi/10.1111/jmg.12759 by Universitat Bern, Wiley Online Library on [13/03/2024]. See the Terms and Conditions (https://onlinelibrary.wiley.com/terms-and-conditions) on Wiley Online Library for rules of use; OA articles are governed by the applicable Creative Commons License

Metamorphic Geology, *18*, 497–511. https://doi.org/10.1046/j.1525-1314.2000.00269.x

White, R. W., Palin, R. M., & Green, E. C. R. (2017). High-grade metamorphism and partial melting in Archean composite grey gneiss complexes. *Journal of Metamorphic Geology*, *35*, 181–195. https://doi.org/10.1111/jmg.12227

White, R. W., Powell, R., & Clarke, G. L. (2002). The interpretation of reaction textures in Fe-rich metapelitic granulites of the Musgrave block, Central Australia: Constraints from mineral equilibria calculations in the system K_2O–FeO–MgO–Al_2O_3–SiO_2–H_2O–TiO_2–Fe_2O_3. *Journal of Metamorphic Geology*, *20*, 41–55. https://doi.org/10.1046/j.0263-4929.2001.00349.x

White, R. W., Powell, R., Holland, T. J. B., Johnson, T. E., & Green, E. C. R. (2014). New mineral activity–composition relations for thermodynamic calculations in metapelitic systems. *Journal of Metamorphic Geology*, *32*, 261–286. https://doi.org/10.1111/jmg.12071

Wiemer, D., Schrank, C. E., Murphy, D. T., Wenham, L., & Allen, C. M. (2018). Earth's oldest stable crust in the Pilbara craton formed by cyclic gravitational overturns. *Nature Geoscience*, *11*, 357–361. https://doi.org/10.1038/s41561-018-0105-9

SUPPORTING INFORMATION

Additional supporting information can be found online in the Supporting Information section at the end of this article.

Table S1. Laser ablation ICP–MS data for selected major and trace elements in garnet. Compositional data is provided (in parts per million) for reference materials NIST-610, NIST-612 and GSD-1G and unknowns AC-13 and AC-12. Analyses for unknowns were collected in grain mounts and across representative garnet grains in thin sections. Limit of detection (LOD) after Howell et al. (2013). bd: below detection.

Table S2. Laser ablation ICP–MS/MS data for Lu–Hf garnet geochronology of sample AC-13. A selection of major and trace elements is analysed to monitor mineral inclusions in garnet. In addition to the inverse notation of Lu–Hf isotope data that have been corrected for an age deviation of the secondary standard (∼3.3%), data is also provided in standard and inverse notation (uncorrected).

Figure S3. Inverse Lu–Hf errorchron age for garnet in sample AC-12 prior to filtering of analyses affected by Paleoproterozoic resetting. Error ellipses are shown at the 2σ level.

How to cite this article: Kaempf, J., Johnson, T. E., Clark, C., Alfing, J., Brown, M., Lanari, P., & Rankenburg, K. (2024). Paleoarchean metamorphism in the Acasta Gneiss Complex: Constraints from phase equilibrium modelling and in situ garnet Lu–Hf geochronology. *Journal of Metamorphic Geology*, *42*(3), 373–394. https://doi.org/10.1111/jmg.12759

15251314, 2024, 3, Downloaded from https://onlinelibrary.wiley.com/doi/10.1111/jmg.12759 by Universitat Bern, Wiley Online Library on [13/03/2024]. See the Terms and Conditions (https://onlinelibrary.wiley.com/terms-and-conditions) on Wiley Online Library for rules of use; OA articles are governed by the applicable Creative Commons License